JACS Au
AN OPEN ACCESS JOURNAL OF THE AMERICAN CHEMICAL SOCIETY

pubs.acs.org/jacsau
Article

Enzymatic Degradation of Deoxynivalenol with the Engineered Detoxification Enzyme Fhb7

Published as part of JACS Au virtual special issue "Biocatalysis in Asia and Pacific".

Jun Yang, Kai Liang, Han Ke, Yuebin Zhang, Qian Meng, Lei Gao, Junping Fan, Guohui Li, Hu Zhou, Junyu Xiao,* and Xiaoguang Lei*

Cite This: JACS Au 2024, 4, 619–634

Read Online

ACCESS | Metrics & More | Article Recommendations | Supporting Information

ABSTRACT: In the era of global climate change, the increasingly severe *Fusarium* head blight (FHB) and deoxynivalenol (DON) contamination have caused economic losses and brought food and feed safety concerns. Recently, an FHB resistance gene *Fhb7* coding a glutathione-S transferase (GST) to degrade DON by opening the critical toxic epoxide moiety was identified and opened a new window for wheat breeding and DON detoxification. However, the poor stability of Fhb7 and the elusiveness of the catalytic mechanism hinder its practical application. Herein, we report the first structure of Fhb7 at 2.41 Å and reveal a unique catalytic mechanism of epoxide opening transformation in GST family proteins. Furthermore, variants V29P and M10 showed that 5.5-fold and 266.7-fold longer half-life time than wild-type, respectively, were identified. These variants offer broad substrate scope, and the engineered biosafe *Bacillus subtilis* overexpressing the variants shows excellent DON degradation performance, exhibiting potential at bacterium engineering to achieve DON detoxification in the feed and biomedicine industry. This work provides a profound mechanistic insight into the enzymatic activities of Fhb7 and paves the way for further utilizing Fhb7-related enzymes in crop breeding and DON detoxification by synthetic biology.

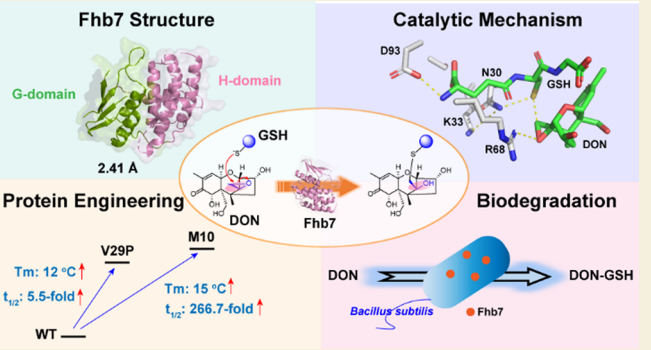

KEYWORDS: *deoxynivalenol degradation, Fhb7, thermal stability, consensus sequence, protein engineering, synthetic biology, Fusarium head blight*

Climate change has emerged as a global concern, giving rise to various biotic stresses that threaten food and feed safety.[1] *Fusarium* head blight (FHB), caused by *Fusarium* species, stands out as one of the most devastating fungal diseases affecting wheat and barley worldwide.[2] As climate change progresses, the incidences of warm and damp weather conditions have increased, exacerbating the severity of FHB.[1,3] This not only leads to substantial economic losses but also contributes to the accumulation of mycotoxins produced by *Fusarium* species, thereby increasing the risks associated with food and feed safety. Consequently, effective control of FHB and mycotoxin detoxification have become imperative in addressing the challenges confronting our food system in the current era of climate change.

Deoxynivalenol (DON), an epoxy-sesquiterpenoid secondary metabolite produced by *Fusarium* species, is an inhibitor of protein synthesis and an essential pathogenic factor of FHB.[4−7] DON contamination has aroused worldwide concerns due to its severe immunotoxicity, cytotoxicity, and genetic toxicity in humans and animals.[8−11] Apart from raw materials infected with FHB, DON contamination can occur during the storage and processing of grains.[12] These factors highlight the critical need to develop an efficient method for degrading DON to ensure food and feed safety. However, the stable structure of DON makes its degradation challenging. Compared with chemical and physical degradation strategies, typically inefficient, unsafety, and prone to nutrition loss, biological methods have received increasing attention owing to their advantages in safety, efficiency, and environmental protection.[13−16] Although several microorganisms capable of DON degradation have been isolated, only a few enzymes that can transform DON into products with lower toxicity have been identified.[8,17−19] While enzymatic transformations

Received: November 8, 2023
Revised: January 19, 2024
Accepted: January 23, 2024
Published: February 12, 2024

targeting C9=C10[20] and C3−OH of DON,[8,18,21] including acetylation,[22−24] glycosylation,[25−28] epimerization, and oxidation,[29−32] have been reported, the discovery of enzymes capable of de-epoxidation holds broader implications, as the epoxy group at C12/C13 is the most critical toxic component of DON[33] (Figure 1A).

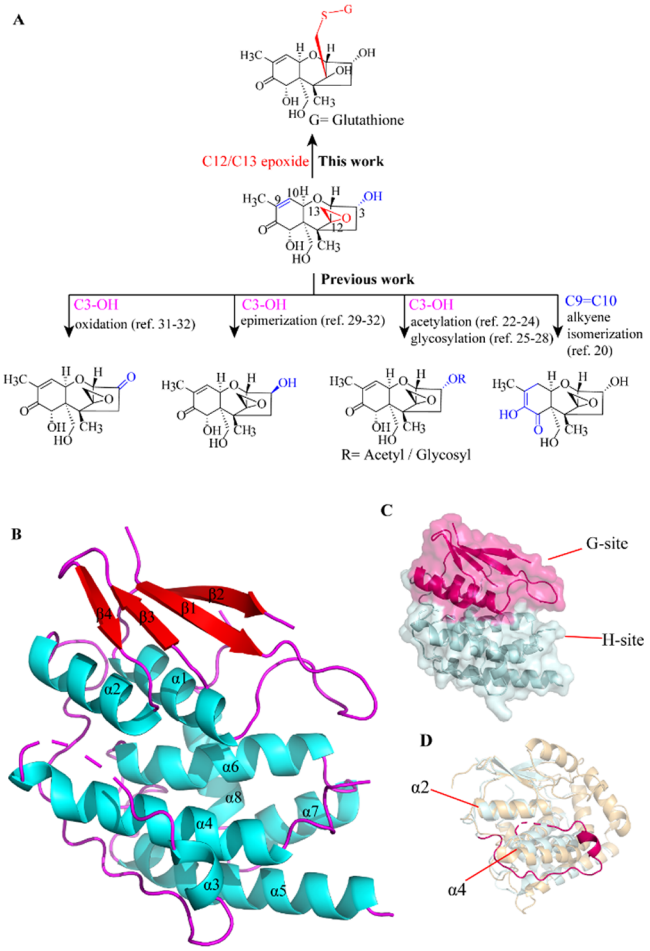

Figure 1. Enzymatic transformations of deoxynivalenol (DON) degradation and the overall structure of Fhb7. (A) Different enzymatic transformations of DON: C3−OH (blue), C9=C10 (blue), and C12/C13 epoxy (red). (B) Overall structure of Fhb7. The α-helices, β-sheet, and loops are shown in cyan, red, and purple, respectively. (C) Fhb7 consists of two different domains: an N-terminal GSH binding domain (G-site, magenta) and a C-terminal hydrophobic binding domain (H-site, pale cyan). (D) Structure comparison of Fhb7 (pale cyan) and CsGST83044 (PDB entry 6J3G, light orange). The long insertion loop of Fhb7 that connects α2 and α4 was highlighted in magenta.

The enzymatic transformation of DON through epoxide opening is particularly challenging due to the inert nature of the epoxy group at C12/C13. Before 2020, only one type of biotransformation targeting this epoxide, performed by anaerobic bacteria from intestines, was discovered.[34] The bacterium *Eubacterium* sp. BBSH 797, derived from bovine rumen fluid, performs reductive de-epoxidation to convert DON to DOM-1,[35,36] and has been used as a feed additive for DON detoxification in the industry.[33] However, despite isolating the pure strain in 1997,[37] the specific enzyme responsible for this transformation has remained elusive for the past three decades. In 2020, a significant breakthrough occurred in identifying Fhb7, the first enzyme to target the inactive C12/C13-epoxy of DON.[38] Fhb7 belongs to the glutathione S-transferase (GST) superfamily and facilitates the opening of the C12/C13-epoxy using glutathione (GSH) as an antidote.[38] The discovery of Fhb7 has garnered considerable attention in wheat breeding due to its importance in FHB resistance. However, the lack of structural information and understanding of the catalytic mechanism of Fhb7 limits further exploration.

The thermostability of enzymes plays a crucial role in their practical application.[39] Enhancing their stability becomes necessary for enzymes with essential functions but low stability to meet the demands of industrial uses. In the case of thermo-unstable Fhb7, thermostability engineering could significantly enhance its potential as a valuable enzyme for DON detoxification in the feed industry. Additionally, it could also reinforce its role as a critical FHB resistance gene in crop breeding. By improving the thermostability of Fhb7, its practical utility and effectiveness could be enhanced, opening up new possibilities for its application in various fields.

Herein, we determined the crystal structure of Fhb7 at 2.41 Å resolution, representing a significant breakthrough as it is the first structure of an enzyme capable of detoxifying enzyme DON by specifically targeting the critical C12/13 epoxy group. We also thoroughly elucidated the catalytic mechanism and the DON binding pocket of Fhb7. These structural and mechanistic information provides valuable insights into its functionality and serves as a solid foundation for further engineering of Fhb7 to expand its substrate scope. Moreover, two Fhb7 variants with desired thermostability, activity, and broad substrate scope were engineered using evolution−sequence-based multitrack strategies. Ultimately, the engineered *Bacillus subtilis* expressing these variants, commonly used as an additive in the feed industry, showed outstanding performance in degrading DON. Overall, our findings shed light on the mechanistic intricacies of Fhb7's enzymatic activities, offering a foundation for further research and application of Fhb7-related enzymes. This work holds immense promise for addressing the challenges posed by DON contamination in both agricultural and industrial settings.

OVERALL STRUCTURE OF FHB7

To gain deep insights into the function of Fhb7, we solved the crystal structure of Fhb7 at 2.41 Å resolution (Figure 1B). The crystallographic analysis revealed that the asymmetric unit contains two Fhb7 molecules, indicating that Fhb7 forms a homodimer in the crystals (Figure S1A). Notably, specific regions within the structural model displayed disorder, including residues 52−78, 136−139, and 167−198 (Figure S1B), attributed to their inherent flexibility. Previously categorized as a member of the fungal glutathione-S transferase etherase-related (GTE) subfamily,[38] Fhb7 shares similarities with other enzymes in the glutathione-S transferase (GST) superfamily. It comprises two distinct domains: an N-terminal glutathione (GSH) binding domain (G-site) and a C-terminal hydrophobic substrate binding domain (H-site) (Figure 1B,C). Compared with the structural homologue CsGST83044 (approximately 32% sequence identity with Fhb7),[40] which has no function of DON detoxification, the G-site of Fhb7 exhibits remarkable similarity (RMSD = 0.705). In contrast, the H-site exhibits notable structural differences (Figure S2A,B). Specifically, Fhb7 features a long flexible loop

https://doi.org/10.1021/jacsau.3c00696
JACS Au 2024, 4, 619−634

(residues 105−140, consisting of 36 residues) inserted between helices α2 and α4, contrasting with the short loop (10 residues) linking the corresponding helices in other family members (Figures 1D and S3). Interestingly, when the length of this loop in Fhb7 was shortened to match that of CsGST83044, the relative activity of Fhb7 decreased to less than 5% (Figure S2C). Collectively, these results underscore the significance of the inserted long loop and structural differences at the H-site, suggesting their involvement in Fhb7's ability to recognize DON and transform it into a nontoxic GSH-DON adduct.

NOVEL ASPARAGINE-BASED ATYPICAL-TYPE ACTIVATION MECHANISM OF GSH IN FHB7

In our efforts to investigate the catalytic mechanism of Fhb7, we employed various strategies to obtain the complete structure of Fhb7 and the complex structure of Fhb7 with its substrates or products. Regrettably, all attempts were unsuccessful due to the inherent flexibility of certain regions within Fhb7 and the weak binding interactions between Fhb7 and its substrates or products. Alternatively, we turned to the Fhb7 variant M10 with higher stability (see below) and its homologue CtGST from *Colletotrichum tofieldiae*, which shares 70% identity and possesses the same catalytic function (Figure S4). The crystal structure of M10 and CtGST was solved at 2.0 and 2.3 Å resolution, respectively, offering additional structural information previously inaccessible in the missing regions (Figure S5A,B and Table S1). Unfortunately, no substrates or products were captured in the complex with CtGST due to the constraints of the crystal lattice, in which a neighboring monomer occupied the active site.

Nevertheless, the structure of CtGST closely resembles that of Fhb7 (RMSD = 0.627), with minor structural differences observed in the flexible α2−α4 loop and the loop following the α1 helix (Figure S5C). We also constructed variant CtGST-F76A to overcome the problem of constraints and solved the crystal structure of CtGST-F76A. However, we still cannot obtain the complex structures.

Using hydrogen−deuterium-exchange mass spectrometry (HDX-MS) of the full-length protein M10, we successfully identified 16−40, 60−80, and 160−190 as the primary regions responsible for GSH binding due to the deuterium uptake profile, which is consistent with the reported GSH binding domain in GST superfamily (Figure S6A−C). To elucidate the catalytic mechanism, we modeled the missing regions of Fhb7 and docked the substrate GSH into the conserved G-site according to the reported cocrystal structure of CsGST83044 (PDB: 6J3H) and the results of HDX-MS. Interestingly, the thiol group of GSH was found to be in close proximity to Asn30 in Fhb7, suggesting that the residue may act as a catalytic site (Figure 2A). The fungal GST superfamily is categorized into four catalytic types based on the residue closest to the thiol group of GSH: tyrosine-, serine-, cysteine-, and atypical-type.[40] Fhb7 belongs to a serine-type GTE subfamily protein, but interestingly, it features an Asn residue near the thiol group of GSH instead of Ser, as observed in other GTE subfamily proteins[38,40−42] (Figure 2A). All these results demonstrate that Fhb7 is an atypical-type GTE subfamily protein that relies on an asparagine-based catalytic mechanism. Notably, two other GST enzymes CsGST83044[40] and CsGST63524[43] from *Ceriporiopsis subvermispora* exhibiting similar features were reported.[40,43,44] CsGST63524 is classified as a serine-type GST where Asn23 and Tyr45 form direct

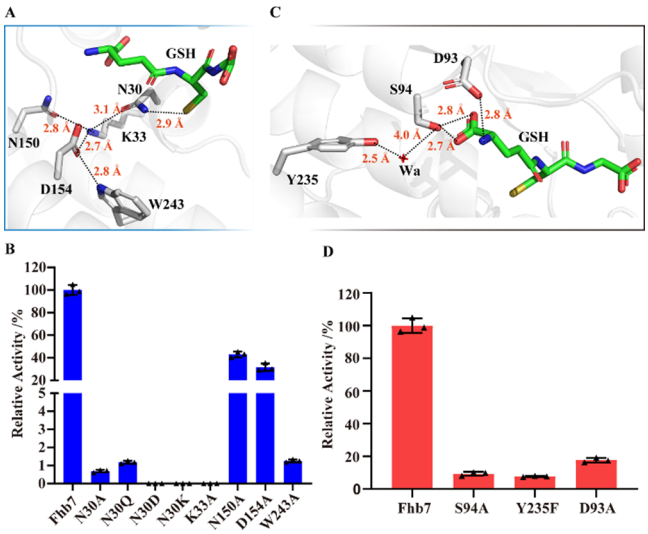

Figure 2. Catalytic mechanism of Fhb7. (A) Structural model of thiol activation. Five residues, N30, K33, W243, N150, and D154, form a hydrogen-bond network to interact with the thiol of GSH. (B) Relative activity of Fhb7 variants proved the importance of the N−K−W−N−D based hydrogen-bond network. (C) Structural model of residues interaction with GSH. Four residues, D93, S94, Y235, and a water molecule form an electron-sharing network to interact with GSH. (D) Relative activity of Fhb7 variants proved the importance of S−Y−D−Wa-based electron-sharing network for catalytic function. All enzymatic reactions were performed in 100 μL of Na_2HPO_4−NaH_2PO_4 buffer (pH 8.0) containing 100 μM DON, 1 mM GSH, and 5 μg Fhb7 or one of its variants at 30 °C for 6 min. All the above data are presented as mean values ± s.d. Error bars represent standard deviations of three independent measurements.

hydrogen bonds with the thiol group (Figure S7A). At the same time, CsGST83044 is considered an atypical-type GST, where Asn22, Asn24, and Tyr46 directly interact with the thiol group of GSH (Figure S7B). For Fhb7, only Asn30 interacts directly with the thiol group, and the hydrogen-bond network between Asn and Tyr observed in CsGST63524 and CsGST83044, which contributes to catalytic function, is replaced by a unique hydrogen-bond network involving Asn30, Lys33, Trp243, Asn150, and Asp154 (N−K−W-N-D) in Fhb7 (Figure 2A). All the mutagenesis to these residues dramatically decreased the catalytic activity, strongly supporting the hypothesis that the hydrogen-bond network plays an important role in opening the epoxy group of DON (Figure 2B and Tables S2 and S3).

In addition, another hydrogen-bond network has been proven to be involved in the catalytic mechanism and occurs widely in different GST superfamilies.[45] However, rare information about the network of the GTE subfamily has been reported. To verify whether the conserved network also exists in Fhb7, we analyzed the amino acids around the glutamyl α-carboxylate of GSH. Residues S94, Y235, D93, and a water molecule form a complicated hydrogen-bond network for the catalytic process (Figure 2C). When the five residues in the network were mutated individually to alanine, the relative activity of each variant decreased dramatically (Figure 2D and Tables S2 and S3), suggesting that the hydrogen-bond network of S−Y−D−Wa promotes the GSH-mediated opening of the inactive epoxide.

https://doi.org/10.1021/jacsau.3c00696
JACS Au 2024, 4, 619−634

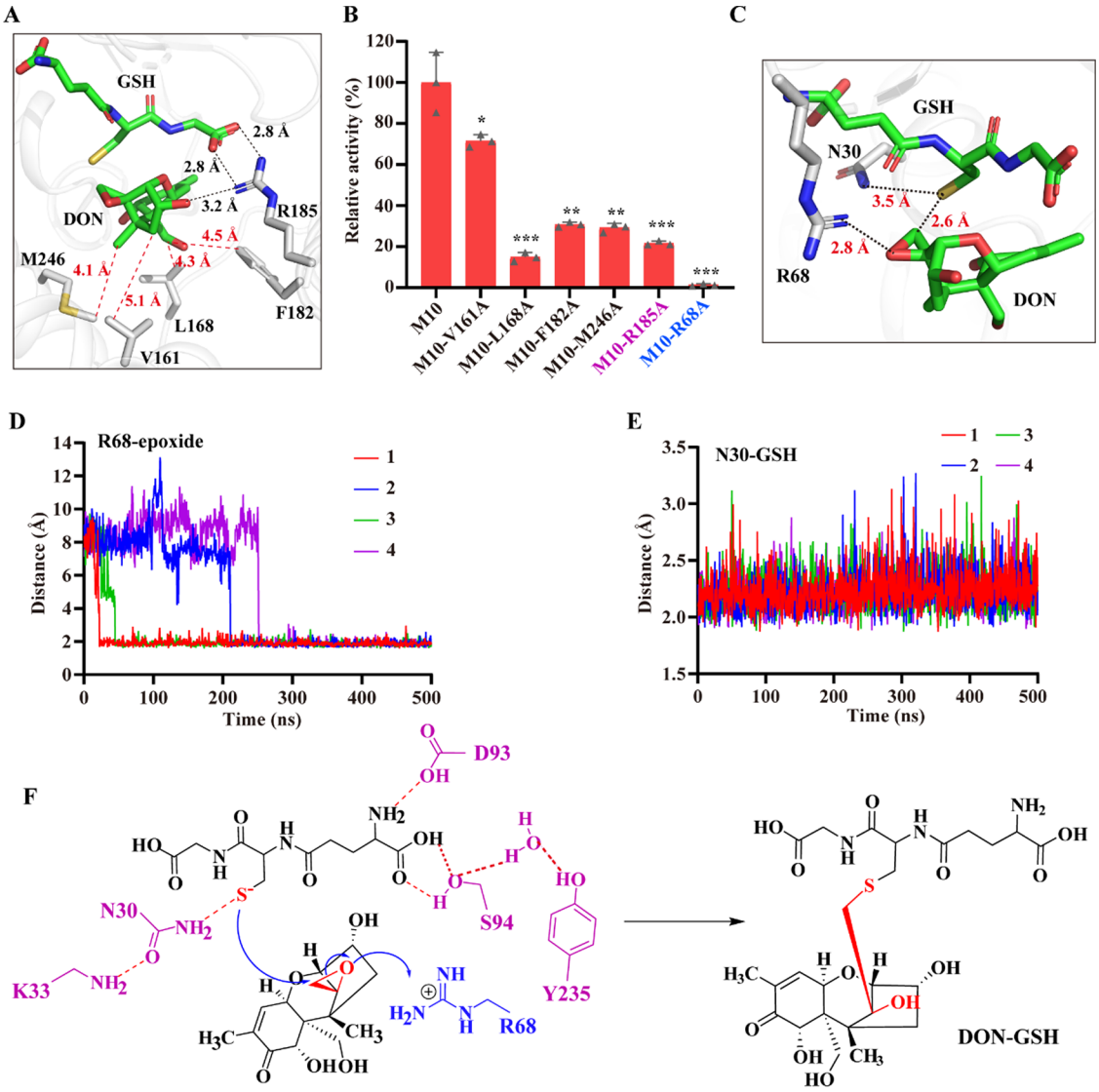

Figure 3. DON binding pocket in Fhb7 and catalytic mechanism of Fhb7. (A) DON binding pocket in Fhb7. The transition state was docked into the substrate pocket and conducted MD simulations. DON binds in a hydrophobic pocket consisting of residues V161, L168, F182, and M246. Residue R185 forms hydrogen-bond interactions with 3-OH of DON and the carboxyl group of GSH. (B) Mutagenesis studies of Fhb7-M10. Enzymatic reactions were performed with 100 μM DON, and 1 mM GSH at pH 8.0 and 30 °C for 6 min in the presence of 5 μg protein. All the above data are presented as mean values ± s.d. Error bars represent standard deviations of three independent measurements. *: $P < 0.05$; **: $P < 0.01$; ***: $P < 0.001$. (C) DON is activated by R68. Residue R68 forms strong hydrogen-bond interactions with the C12/C13 epoxy group of DON in the MD simulations. N30 interacts with a sulfur atom of GSH during the simulations. (D) Distances between R68 and C12/C13 epoxide of DON. R68 began interacting with the epoxide and maintained strong interactions during all the simulations. (E) Distances between N30 and thiol group of GSH. During the four independent MD simulations, the distances between N30 and the thiol group of GSH were shorter than 3.5 Å all the time. (F) Proposed catalytic mechanism of Fhb7. S−Y−D−Wa based hydrogen-bond network interacts with glutamyl α-carboxylate to promote the production of the sulfur anion, and N−K−W−N−D-based hydrogen-bond network stabilizes the anion. R68 activates the epoxide of DON, and the sulfur anion attacks the C12/C13 epoxide to produce the final adduct product DON-GSH.

CATALYTIC MECHANISM OF EPOXIDE OPENING BY FHB7

Identifying the binding pocket of DON in Fhb7 is challenging due to the nonconserved nature of the H-site in the GST superfamily. We employed molecular dynamics (MD) simulation and HDX-MS to elucidate the binding pocket to overcome this. However, the HDX-MS experiment failed due to Fhb7's extreme instability. To address this issue, we engineered Fhb7 to enhance the stability (referred to as M10, see below) and utilized this variant for further assays. Based on the HDX-MS results, we confirmed that regions 60−80 and 160−190 are the predominant regions of Fhb7 that have a deuterium uptake profile sensitive to DON (Figure S6D,E). Most of the regions belong to the H-site (Figure S6F). Additionally, we conducted 500 ns independent MD simulations with the transition state of the reaction docked into the binding pocket (Figure S8A,B). Interestingly, DON remained stably bound in the substrate pocket throughout all simulations (Figure S8C). Residues V161, L168, F182, and M246 formed a hydrophobic bowl-shaped pocket facilitating hydrophobic interactions with DON (Figures 3A and S7D). Additionally, residue R185 forms hydrogen-bond interactions with 3-OH of DON and the carboxyl group of GSH (Figure 3A). Alanine mutations of these residues significantly

https://doi.org/10.1021/jacsau.3c00696
JACS Au 2024, 4, 619−634

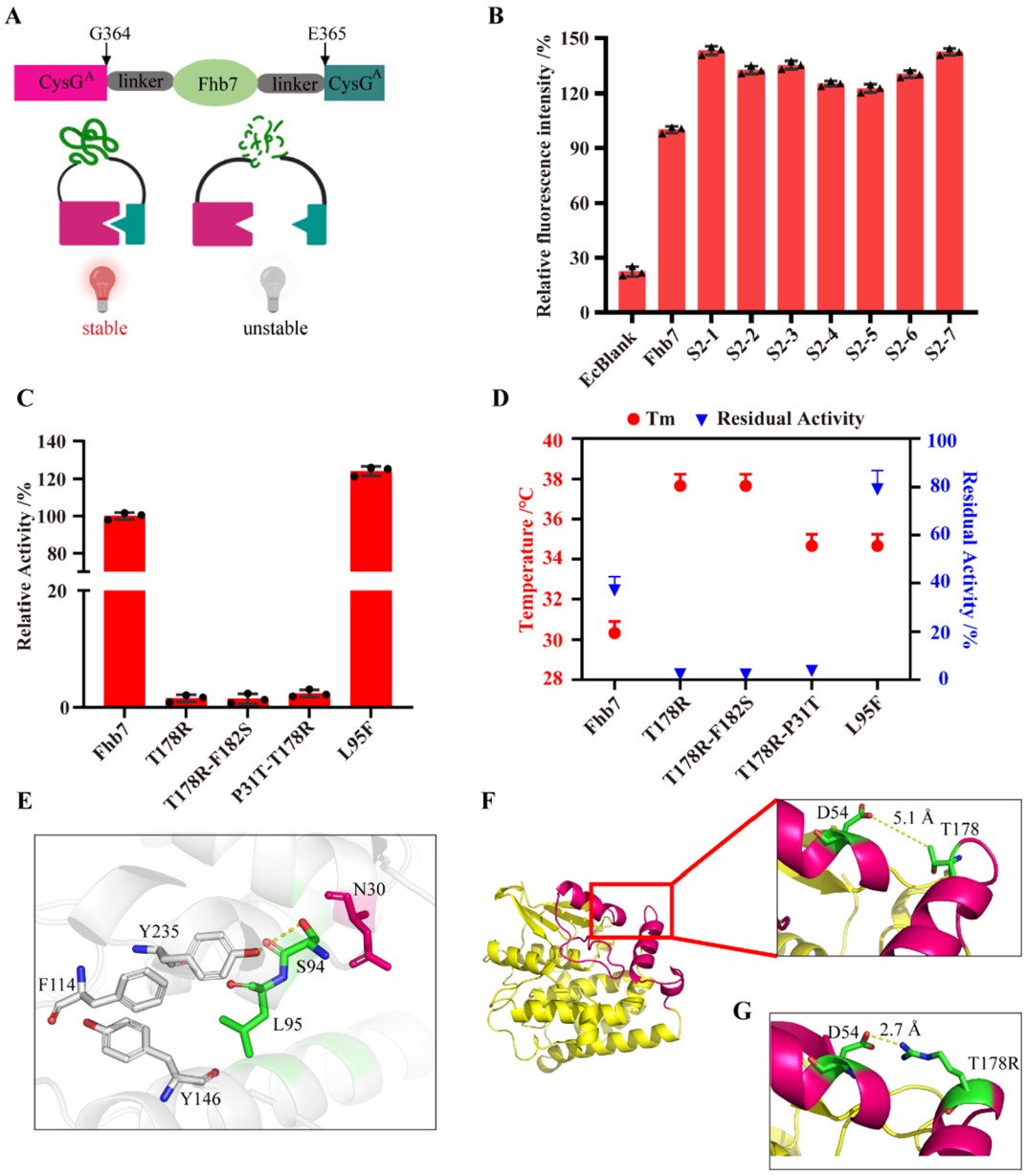

Figure 4. High-throughput screening strategy for thermostability engineering of Fhb7. (A) Biosensor used for high-throughput screening of Fhb7 random mutagenesis library. The gene Fhb7 was inserted after residue G364 of $CysG^A$ with an N-terminal linker SSGSSG and a C-terminal linker GGGGSGGGGS. When the biosensor was transformed into *E. coli* MC1061, variants with higher stability will produce red fluorescence due to the two separated domains of $CysG^A$ reconstituting a functional protein. In comparison, those variants with lower stability will have low fluorescence. (B) Relative fluorescence intensity of variants screened in step II. The fluorescence intensity is determined with an automated plate reader (excitation filter at 360 nm and emission filter at 620 nm). The data represent the mean ± s.d., as determined from three independent measurements. Error bars represent the standard deviations of three independent measurements. (C) Activity of the variants with increasing stability. Enzymatic reactions were performed with 100 μM DON, and 1 mM GSH at pH 8.0 and 30 °C for 6 min in the presence of 5 μg protein. The data represent the mean ± s.d., as determined from three independent measurements. Error bars represent the standard deviations of three independent measurements. (D) Tm value and residual activity of variants. Five different variants were screened from the mutagenesis library, and the Thermofluor assay determined the Tm value of those variants. The residual activities of those enzymes were determined by measuring the activities of enzymes incubated at 30 °C for 5 min relative to the activities of enzymes with no incubation using 0.1 mM DON and 1 mM fresh GSH as substrates. The data represent the mean ± s.d., as determined from three independent measurements. Error bars represent the standard deviations of three independent measurements. (E) Surrounding environment of L95 in Fhb7. L95 is surrounded by three aromatic residues, F114, Y146, and Y235. (F, G) Variants contain T178R form salt-bridge with D54. Residue D54 in wild-type Fhb7 is about 5.1 Å far away from residue T178 (F), while D54 forms a strong salt bridge with mutated Arg in the variants containing T178R (G).

decreased their activity, suggesting their importance in DON bonding (Figure 3B and Tables S2 and S3). Of note, according to the results of MD simulations, the distance between DON and V161 is longer than that between L168, F182, and M246. This suggests a less important role of V161 in binding DON, providing a possible explanation for the higher activity observed in V161A compared to L168A, F182A, and M246A.

Remarkably, during the simulation trajectories, we observed strong hydrogen-bond interactions between residue R68 and the epoxy group of DON, implying the role of R68 in

https://doi.org/10.1021/jacsau.3c00696
JACS Au 2024, 4, 619−634

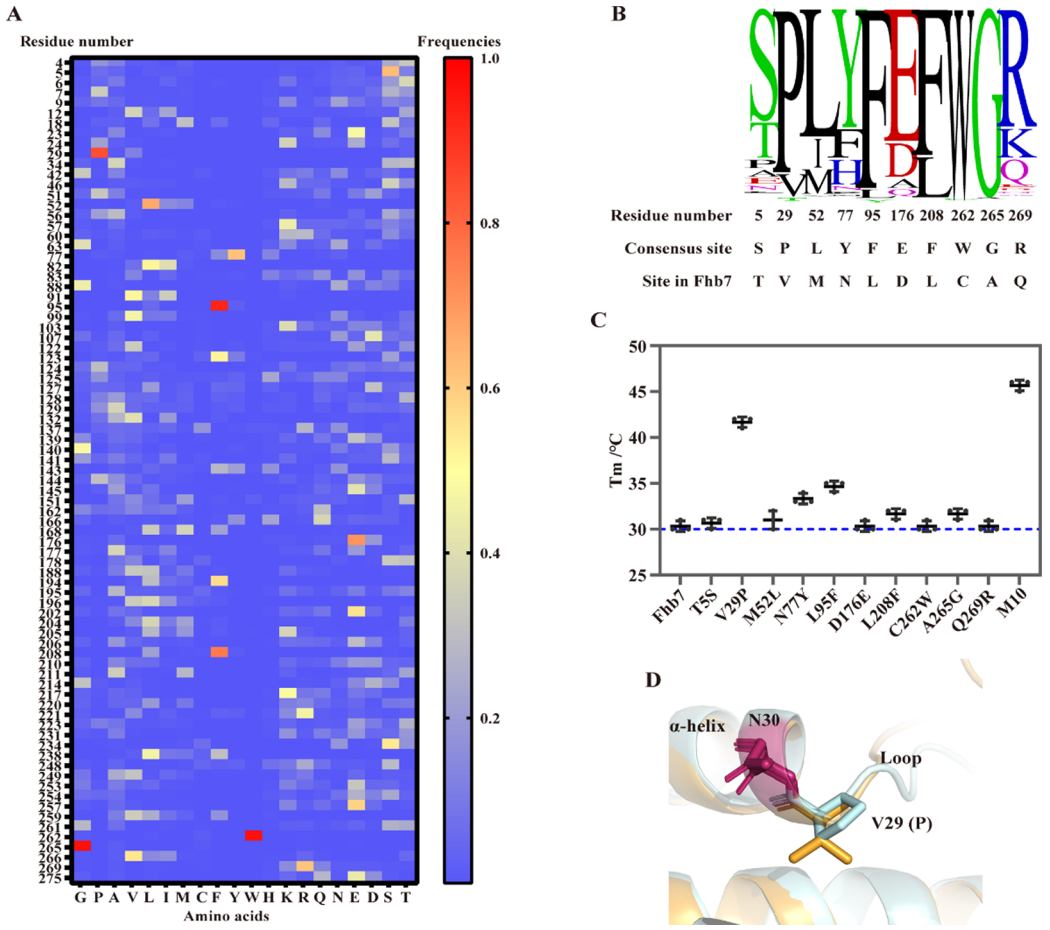

Figure 5. Sequence-based thermostability engineering of Fhb7. (A) Frequencies of amino acids in those positions where residues of Fhb7 are different from the consensus sequence. (B) Construction of a small library with high quality according to the frequencies of amino acids. The variants construction rule replaces the single residue of Fhb7 with the corresponding residue in the consensus sequence. (C) Tm value of the variants. Tm values of the 10 single mutations and a combinatorial mutant M10 were conducted using a Thermofluor assay. The data represent the mean ± s.d., as determined from three independent measurements. Error bars represent the standard deviations of three independent measurements. (D) V29P plays an essential role in the stability of Fhb7. V29 connects the α-helix containing catalytic center N30 and the flexible loop.

activating the epoxy group (Figure 3C,D). Indeed, the catalytic activity was entirely lost when R68 was mutated to alanine (Figure 3B). Moreover, residue N30 of Fhb7 consistently interacts with the thiol group, potentially stabilizing the sulfur anion and promoting the reaction (Figure 3C,E). Therefore, based on these findings, we proposed the mechanism of Fhb7-mediated epoxide opening: the S−Y−D−Wa hydrogen-bond network lowers the pK_a value of GSH's thiol group, and the N−K−W−N−D hydrogen-bond network stabilizes the sulfur anion. Furthermore, R68 carrying a positive charge activates the epoxide of DON, facilitating the ring opening (Figure 3F).

EVOLUTION-BASED STRATEGY FOR THERMOSTABILITY ENGINEERING OF FHB7

Notably, when Fhb7 was purified from *E. coli* lysate, even though all procedures were conducted on ice, the protein exhibited a propensity to precipitate within 10 min at a concentration exceeding 1 mg/mL (Figure S9A), indicating the poor thermostability of Fhb7. Consequently, improving the thermostability of Fhb7 through protein engineering assumes significant importance, as it holds the potential to enhance the practical value and applicability of this enzyme greatly.

In order to improve the thermal stability of Fhb7, we employed a fluorescence sensor for protein engineering. CysG^A is a SAM-dependent methyltransferase that catalyzes the transformation of uroporphyrinogen III to trimethylpyrrocorphin, resulting in red fluorescence under ultraviolet light (Figure S9B). A sandwiched protein stability biosensor based on CysG^A was constructed for the directed evolution of Fhb7 as described in previous research.[46] Initially, the gene encoding Fhb7 was inserted after G364 of CysG^A with an N-terminal linker and a C-terminal linker (Figure 4A). When the fusion protein CysG^A-Fhb7 was overexpressed in *E. coli* MC1061 (EcCF), it emitted bright red fluorescence upon exposure to ultraviolet light, while *E. coli* MC1061 containing empty vector pTrc99a (EcBlank) exhibited no fluorescence (Figure S9C). To evaluate the potential of this biosensor for high-throughput screening in the directed evolution of Fhb7, we measured the fluorescence intensity of EcCF at different temperatures. As the stability of Fhb7 is known to be temperature-sensitive, the relative fluorescence intensity of EcCF gradually decreased from 100% at 30 °C to 65% at 42 °C. In contrast, EcBlank displayed no significant change in fluorescence intensity under the same condition (Figure S10A). These results demonstrate the effectiveness of the CysG^A-based sandwiched biosensor as

https://doi.org/10.1021/jacsau.3c00696
JACS Au 2024, 4, 619−634

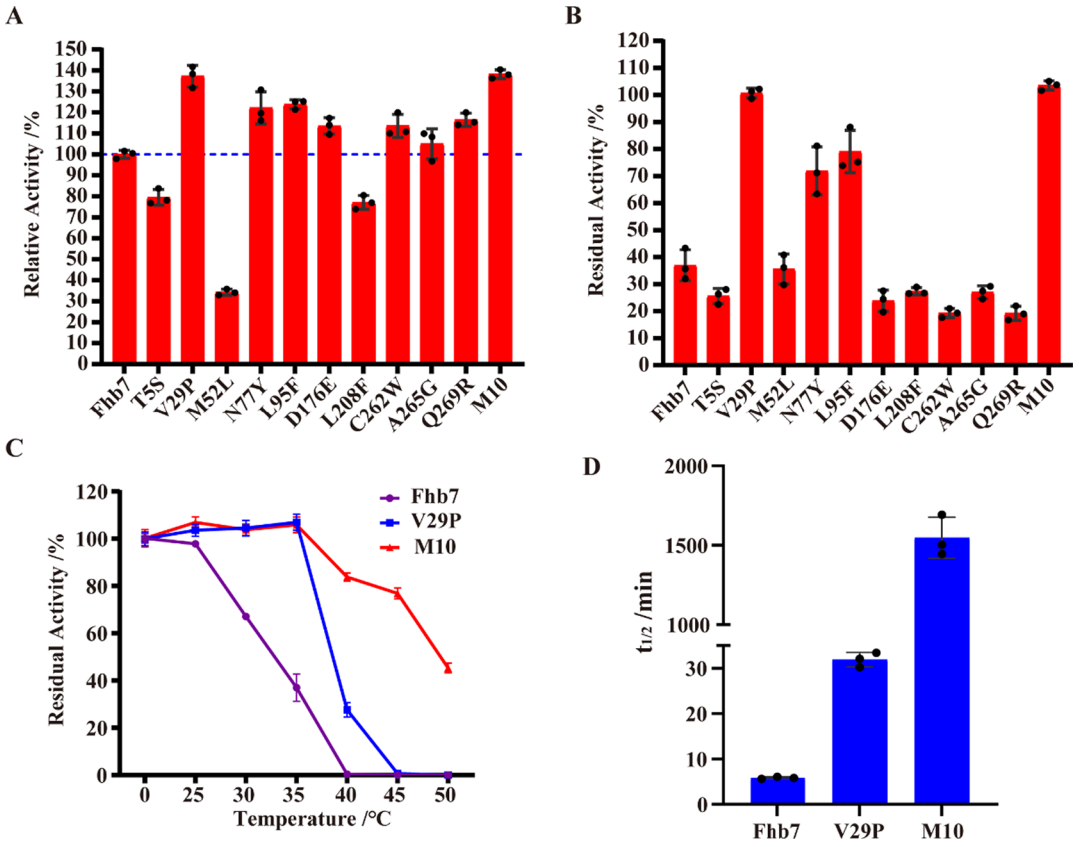

Figure 6. Activity and thermostability of Fhb7 variants and its homologues. (A) Relative activity of variants. Enzymatic reactions for relative activity determination of 10 single variants and a combinational mutation M10 were carried out in the standard condition. (B) Residual activity of the variants. 5 μg proteins in 100 μL of Na_2HPO_4–NaH_2PO_4 buffer (pH 8.0) were incubated at 35 °C for 5 min before activity determination. The reactions were conducted in the standard condition. Residual activity is present as the activity of heated enzymes relative to the activity of enzymes without heating using 0.1 mM DON and 1 mM fresh GSH as substrates. (C) T50 determination of Fhb7, V29P, and M10. The residual activity of Fhb7, V29P, and M10 after incubation at different temperatures for 5 min was determined with the above method. (D) Half-life ($t_{1/2}$) of Fhb7, V29P, and M10. Detection of $t_{1/2}$ was done by determining the residual activity of Fhb7 or its variants incubated at 30 °C for a different time under the standard condition. All the above data represent the mean ± s. d., determined from three independent experiments.

a valuable tool for assessing the stability of Fhb7 during directed evolution experiments.

A three-step high-throughput screening strategy was employed for the directed evolution of Fhb7 (Figure S11): in step I, different Fhb7 variants were expressed in strains containing the biosensor, resulting in colonies displaying a range of red fluorescence intensities under UV light (Figure S10B). From a library of 10^4 variants, 150 colonies with the most intense red coloration were selected. In step II, seven variants exhibiting enhanced fluorescence intensity were chosen from the 150 colonies obtained in step I (Figure 4B). These selected variants contain two T178R, P31T-T178R, L95F, and one T178R-F182S (Table S4). In step III, four different variants from step II were rescreened based on activity to avoid the stability-activity trade-off, which usually occurs in the stability engineering of proteins.[47−49] Surprisingly, all three variants harboring T178R mutation almost completely lost the catalytic function, while L95F maintained 23% higher activity than the wild-type at 30 °C (Figure 4C). Additionally, after a 5 min incubation at 35 °C, variant L95F retained 79% activity, whereas the wild-type retained only 37% (Figure 4D). Furthermore, compared to the wild-type, the Tm values of these variants were observed to be 5−8 °C higher (Figure 4D).

Residue L95 is surrounded by several aromatic amino acids, including Y235, Y146, and F114. When L95F was mutated to phenylalanine, we proposed that phenylalanine may form π−π interaction with the neighboring aromatic residues, improving stability (Figure 4E). T178 is situated in a flexible region of Fhb7 and when it was mutated to Arg, a strong salt bridge interaction is likely formed with Asp54, which is located in the adjacent flexible α-helix (Figure 4F,G). This salt bridge interaction may effectively lock the two flexible α-helices into a stable conformation, thereby significantly increasing the thermostability of Fhb7 (Figure S12A−D). However, due to the rigidification of these regions, T178R mutation results in a loss of function, likely because the flexibility of this region is essential for substrate entry and/or product exit.

SEQUENCE-BASED STRATEGY FOR THERMOSTABILITY ENGINEERING OF FHB7

At a given site in a protein, a consensus amino acid is considered a more critical residue contributing to protein stability than nonconserved amino acids.[50,51] Furthermore, many successful examples of stability and activity engineering have showcased the reliability of consensus site analysis in protein engineering.[50−52] Based on the above, we employed a consensus site-searching strategy to engineer Fhb7 further.

https://doi.org/10.1021/jacsau.3c00696
JACS Au 2024, 4, 619−634

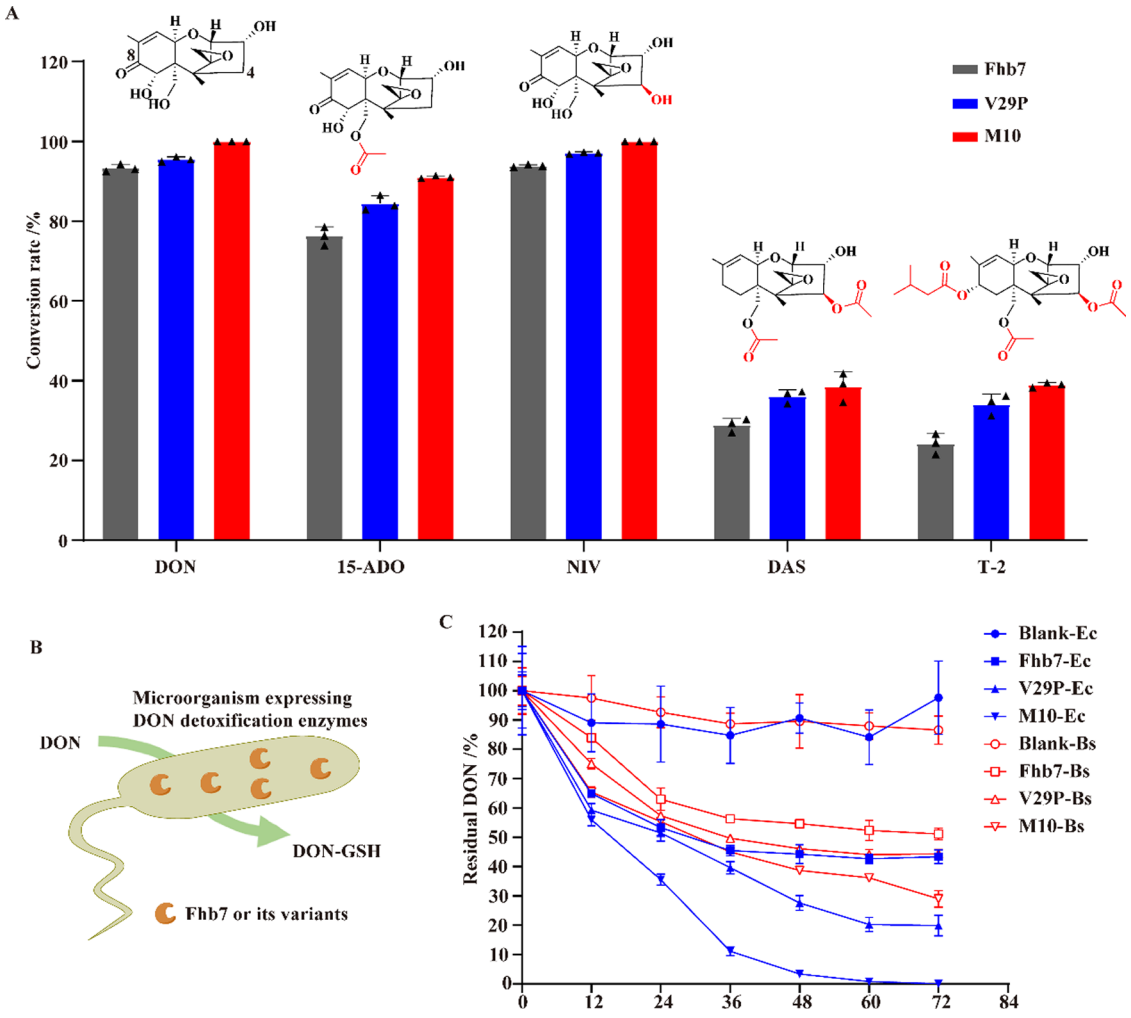

Figure 7. Substrate scope of Fhb7's variants and DON detoxification with the engineered bacteria. (A) Substrate scope of Fhb7, V29P, and M10. Five trichothecene mycotoxins deoxynivalenol (DON), 15-acetyl-deoxynivalenol (15-ADON), nivalenol (NIV), diacetoxyscirpenol (DAS), and T-2 toxin were chosen for substrate scope determination. (B) Engineered microorganisms for biodegradation of DON. (C) DON detoxification in *E. coli* MC1061 (Ec) and *Bacillus subtilis* WB600 (Bs). The detoxification efficiency was determined by detecting the percentage of residual DON in the reaction systems after incubation from 0 to 72 h. All the above data are presented as mean values ± s.d. Error bars represent the standard deviations of three independent measurements.

Using the protein sequence of Fhb7 as a query, 350 homologous sequences were retrieved from the NCBI nonredundant protein database using the Consensus Finder web tool (http://kazlab.umn.edu).[53] These sequences were then subjected to consensus sequence analysis. According to the frequencies of amino acids at each position, 81 sites where the residues in Fhb7 differed from the consensus residues were retrieved (Figure 5A). Subsequently, 10 sites with consensus site frequencies higher than 0.6 were selected for experimental verification (Figure 5B). Ten single mutations (T5S, V29P, M52Y, N77Y, L95F, D176E, L208F, C262W, A265G, and Q269R) were constructed based on the principle of replacing intrinsic residues of Fhb7 with consensus residues. Notably, substitution L95F, which exhibited a 5 °C higher Tm value than the wild-type, has been screened twice from a random mutation library during directed evolution (Figure 4D and Table S4). To avoid overlooking potential beneficial cooperative interactions between substitutions, we combined all 10 consensus substitutions in Fhb7 to generate the variant M10.

Among the 10 single mutations, most variants (V29P, M52L, N77Y, L95F, L208F, A265G) displayed Tm values ranging from 1 to 12 °C higher than Fhb7 (Figure 5C). Surprisingly, introducing a single mutation V29P into Fhb7 increased its Tm value from 30 to 42 °C, highlighting the essential role of this position in the thermostability of Fhb7. V29, located below the active center N30, plays a crucial role in linking the α-helix containing N30 and a flexible loop. Thus, the substitution of Val with the rigid residue Pro reduces the flexibility of this linkage, thereby improving the thermal stability and catalytic activity of Fhb7 (Figure 5D). As for the combinatorial mutation M10, the Tm value is 15 °C higher than wild-type and 3 °C higher than variant V29P (Figure 5C), demonstrating the beneficial cooperative interactions among the selected residues in improving stability.

To validate whether the catalytic functions of those mutations were reserved, we determined the relative activity of those mutations at 30 °C. Four variants V29P, N77Y, L95F, and M10 with Tm values more than 3 °C higher than Fhb7 displayed higher activity than the wild-type. In contrast, other variants with similar Tm values only exhibited slightly higher

https://doi.org/10.1021/jacsau.3c00696
JACS Au 2024, 4, 619−634

relative activity, except M52L, which showed a decrease to 34% activity (Figure 6A). Moreover, after a 5 min incubation at 35 °C, V29P and M10 maintained nearly 100% activity, while N77Y and L95F maintained 72 and 79%, respectively (Figure 6B). However, the other 7 variants retained less than 36% (Figure 6B). Therefore, V29P and M10 were chosen for further exploration due to their superior stability and activity.

To explore their thermal tolerance, Fhb7, V29P, and M10 were incubated at different temperatures for 5 min and their retained activities were determined. Fhb7 maintained 98% and 66% activity after incubation at 25 and 30 °C, respectively, while the catalytic function of Fhb7 was lost when the temperature exceeded 40 °C (Figure 6C). Variants V29P and M10 exhibited a gradual decrease in activity as the incubation temperature increased, but retained nearly 100% activity when the temperature was below 35 °C (Figure 6C). Interestingly, V29P almost entirely lost its function after incubation at 45 °C, while M10 retained 77% residual activity, and even at 50 °C, 19% activity remained (Figure 6C). Half-life ($t_{1/2}$) of Fhb7, V29P, and M10 were assessed by determining the residual activity of these proteins after preincubation at 30 °C for different periods. Surprisingly, the $t_{1/2}$ of Fhb7 is only 5.8 min, indicating relatively low thermostability, while V29P and M10 showed approximately 5.50- and 267-fold longer than Fhb7, respectively (Figure 6D). These results demonstrated the higher thermostability and activity of V29P and M10.

To confirm whether the beneficial effect of substituting Val with Pro at the position corresponding to V29 of Fhb7 (Re29) applies to other homologous proteins, a GST superfamily protein from *Pseudogymnoascus* sp. 05NY08 (PsGST) with Val at Re29, as well as three proteins from *Colletotrichum tofieldiae* (CtGST), *Mortierella* sp. GBA 30 (MsGST) and *Nannizzia gypsea* CBS 118893 (NgGST) with Pro at Re29 were heterologously expressed and purified (Figure S13A). CtGST, MsGST, and NgGST are characterized by higher thermostability and PsGST characterization showed a lower Tm value (Figure S13B). Furthermore, it is noteworthy that the substitution of Val with Pro at Re29 in PsGST increases its Tm value, while the corresponding substitutions in CtGST, MsGST, and NgGST lead to decreased stability (Figure S13C). Additionally, all four above enzymes can detoxify DON as Fhb7, suggesting a widespread distribution of enzymes that can open the C12/C13 epoxy group of DON in fungi (Figure S4). Val29 is located in the relatively conserved N-terminal GSH binding domain and mutation of Val to Pro has no negative impact on activity V29P mutation in Fhb7 and could serve as a guiding example for thermostability engineering of other GST superfamily proteins.

SUBSTRATE SCOPE OF V19P AND M10

Trichothecenes are a large family of mycotoxins produced by various filamentous fungal species such as *Fusarium*, Trichothecium, and Trichoderma.[13] Like DON, all family members are characterized by a special toxic group C12/C13 epoxide.[4] Among trichothecenes, the T-2 toxin is regarded as the most poisonous mycotoxin.[54] Fhb7 has been confirmed as a catalyst that can degrade type A and B trichothecenes with a broad substrate scope.[38] To further investigate the application potential of V29P and M10, we examined their substrate scope using five types of A and B trichothecenes as substrates: deoxynivalenol (DON), 15-acetyl-deoxynivalenol (15-ADON), nivalenol (NIV), diacetoxyscirpenol (DAS) and T-2 toxin. Both V29P and M10 demonstrated higher activity than the wild-type enzyme against all the tested substrates (Figure 7A). Among the five substrates, the conversion rates of V29P and M10 toward DON, 15-ADON, and NIV are more than 83%, while the conversion rates toward DAS and T-2 toxin are below 40% (Figure 7A). These findings showed that the acetylation of C4 negatively affects the recognition of substrates by Fhb7. Collectively, V29P and M10 exhibited higher stability while maintaining a broad substrate scope, demonstrating the enhanced application potential achieved through the engineering of Fhb7.

DEOXYNIVALENOL DETOXIFICATION *IN VIVO*

Due to the limited environmental tolerance of purified enzymes, various limitations often hinder their application *in vitro*. When it comes to enzymes involved in mycotoxin detoxification, they are commonly used as additives in feed or food storage. This working environment makes it difficult for purified enzymes to maintain their enzymatic activity and stability. To overcome this obstacle, replacing purified proteins with probiotics containing mycotoxins detoxifying genes has emerged as a promising solution in practical applications. Although several microorganisms capable of DON detoxification have been identified, their utilization is limited due to safety concerns. Hence, engineering a biosafe bacterium carrying mycotoxins detoxifying genes becomes an alternative strategy.[55] However, no previous examples of engineering probiotics for mycotoxin detoxification have been reported. To investigate the potential use of Fhb7 and its mutants as gene bricks for constructing engineered strains, we overexpressed the genes in *E. coli* MC1061 and *Bacillus subtilis* WB600 (Figure 7B). The target proteins can be expressed successfully using *E. coli* and *B. subtilis* as chassis cells with high expression levels (Figure S14A,B). Owing to the difference in stability, protein expression of M10 was 40% and 2-fold higher than wild-type in *E. coli* and *B. subtilis*, respectively (Figure S14C). Meanwhile, V29P showed comparable protein expression levels with Fhb7 in both expression systems (Figure S14C). Using strains overexpressing Fhb7 or variants as additives, successful *in vivo* degradation of DON was achieved (Figure 7C). For *E. coli* MC1061, after 72 h incubation at 37 °C, no detectable DON remained in the strain expressing M10 (M10-Ec), while approximately 80% DON was metabolized by V29P-Ec (strain overexpressing V29P). In contrast, Fhb7-Ec (strain overexpressing Fhb7) degraded only 55% of DON (Figure 7C). Moreover, V29P-Ec exhibited sustained degradation after 60 h, whereas Fhb7-Ec lost its DON metabolism capability after 36 h (Figure 7C). For *B. subtilis* WB600, although the degradation efficiencies are lower than *E. coli* MC1061, the overall trend of DON degradation was similar (Figure 7C).

About 51, 56, and 72% of DON were metabolized by *B. subtilis* WB600 overexpressing Fhb7, V29P, and M10, respectively, within 72 h (Figure 7C), demonstrating that M10 showed higher DON degradation efficiency in *B. subtilis* than wild-type. All the above results support the notion that thermostability engineering of Fhb7 improves its enzymatic characteristics for practical application. The stable variant can serve as a gene brick to construct an engineered bacterium with trichothecenes detoxification capabilities.

https://doi.org/10.1021/jacsau.3c00696
JACS Au 2024, 4, 619−634

DISCUSSION

We have solved the first crystal structure of Fhb7, an unprecedented enzyme that metabolizes DON into a nontoxic product, by opening the C12/C13 epoxide, the most toxic group in DON. Our work also illustrates a novel GSH activation mechanism of Fhb7 in which the N−K−W−N−D− and S−Y−D−R−Wa-based hydrogen-bond networks work together to decrease the pK_a of the thiol of GSH and further promote enzymatic transformation. DON is the main mycotoxin from *Fusarium* sp. and not only brings health concerns[10] but also plays a significant role in the spread of FHB.[7] With the disclosure of structure information and understanding of the catalytic mechanism, the application value of the enzyme will be further improved via rational engineering or directed evolution to enhance the activity and environmental suitability of Fhb7.

For those proteins with important function and application value but low stability, thermostability becomes the critical factor limiting their application in practice. This study identified two substitutions, V29P and M10, using an evolution-sequence-based thermostability engineering strategy. Due to the expense and difficulty of obtaining DON, a CysG^A-based biosensor was used for Fhb7-directed evolution according to stability instead of activity, significantly decreasing the consumption of DON. Functional variants such as L95F were also obtained using this method. For sequence-based engineering strategy, the Consensus Finder tool was used to analyze the amino acid frequencies and construct a library with high quality according to the consensus sites. In all the above engineering methods, we successfully engineered Fhb7 while consuming minimal expensive substrate. The engineering strategy may also be suitable for the stability engineering of other enzymes whose substrate is difficult to obtain. The successful thermostability engineering of Fhb7 not only endows it with higher value in crops breeding with higher FHB resistance but also makes it possible to use Fhb7 as a safe, highly efficient, and environmentally friendly DON detoxification catalyst in the feed industry.

DON contamination is a severe problem in the feed industry and causes significant economic loss. Biological detoxification strategies have shown promising application potential due to their advantages of safety, eco-friendliness, high selectivity, and high efficiency. In this study, *Bacillus subtilis*, commonly used as feed additives in industry, was engineered to transform DON *in vivo* successfully. To our knowledge, this is the first example of using a synthetic biological strategy to construct engineering probiotics for DON detoxification. Engineering probiotics using those genes encoding DON degradation enzymes as gene bricks can not only overcome the biosafety concerns from other detoxifying microorganisms but also solve the current problem of environmental tolerance of these enzymes when used *in vitro*. Besides DON, many other mycotoxins, such as aflatoxin and zearalenone, are also notorious in the industry. Using the synthetic biological strategy, it is possible to construct an engineering microorganism to degrade almost all the mycotoxins. We expect that this work may provide a valuable tool and a new strategy for solving the problem of mycotoxin contamination in the industry.

METHODS

General

Primer and gene synthesis was conducted at Generay Biotech Co. Ltd. DNA sequencing was performed at RuiBiotech Company. ClonExpress II One Step Cloning Kit was purchased from Vazyme Biotech. PCR to obtain DNA fragments was carried out using standard thermos cycling protocols with TransStart FastPfu DNA polymerase (Transgene Biotech) and MEGAWHOP PCR was conducted using KOD-Plus-Neo polymerase purchased from TOYOBO. Error-prone PCR was performed using rTaq DNA polymerase (Vazyme Biotech). All protein quantification was performed using a NanoDrop 2000 Spectrophotometer (Thermo). The analysis of enzymatic reaction products was performed on an ACQUITY ultraperformance liquid chromatography (UPLC) H-class system (Waters) coupled with an SQ Detector 2 equipped with an electrospray ionization source. All the UPLC/mass spectrometry (MS) analysis was conducted on an ACQUITY UPLC BEN C18 column (length, 50 mm; inner diameter, 2.1 mm; particle size, 1.7 μm; Waters) at a flow rate of 0.3 mL per minute at 40 °C. The gradient elution consists of 0.1% formic acid (A) and MeCN (B). The gradient programs were 100% A, 0−0.5 min, 100−98% A, 0.5−1 min, 98−95% A, 1−2.5 min, 95−60% A, 2.5- 4.5 min, 60−10% A, 4.5−6.5 min, 10% A, 6.5−8.0 min.

Plasmid Construction

All the linear vectors pQlinkHx, pQlinkMx, pMA5, and pTrc99a used to construct the following plasmids were obtained by PCR using corresponding primers listed in Supplementary Table 5. For protein expression and purification for activity and Tm value test, the genes were cloned into vector pQlinkHx. The DNA fragments of Fhb7, CtGST (NCBI accession KZL73730.1), PsGST (NCBI accession OBT73859.1), NgGST (NCBI accession XP_003171787.1), and MsGST (NCBI accession KAG0211024.1) were obtained by PCR with TransStart FastPfu DNA polymerase (Transgene Biotech) using synthesized genes as templates and corresponding primers. The DNA fragments were linked into linear vector pQlinkHx, respectively, using a ClonExpress II One Step Cloning Kit (Vazyme Biotech) with standard protocol. For crystallization, the DNA fragment of Fhb7 was linked into linear vectors pQlinkMx as described above. For biosensor construction for high-throughput screening of the Fhb7 random mutagenesis library, we amplified the gene of CysG^A from the genome of *E. coli* MC1061 with PCR using primers pTrc99a-CysG^A-F and pTrc99a-CysG^A-R. The plasmid pTrc99a-CysG^A was constructed successfully using the ClonExpress II One Step Cloning Kit. We obtained a new linear vector via PCR using plasmid pTrc99a-CysG^A as a template and 99a-CysG^A-F and 99a-CysG^A-R as primers. A DNA fragment of Fhb7-CysG^A, obtained by PCR using plasmid pQlinkHx-Fhb7 as template and Fhb7-CysG^A-F/R as primers, was linked into the new linear vector described above. For plasmids used for overexpression of Fhb7, V29P, and M10 in *Bacillus subtilis* WB600, gene fragments of Fhb7, V29P, and M10 were obtained from plasmids containing the gene of Fhb7, V29P, or M10 by PCR using Fhb7-His-F and Fhb7-His-R as primers. These fragments were linked into linear vector pMA5 as described above. All the primers used in this study are presented in Table S5.

Protein Expression and Purification of Fhb7 and CtGST for Crystallization

For expression of recombinant protein Fhb7, the synthesized Fhb7 gene was cloned into a pQlinkMx vector with an N-terminal MBP tag followed by an additional 8xHis tag and TEV cleavage site. Protein expression was performed with *E. coli* BL21 harboring pQlinkMx-Fhb7. Cells were grown at 37 °C to an OD600 value of 0.8−1.0 and induced at 16 °C by 1 mM IPTG for 20 h. Cells were harvested and lysed by high-pressure homogenization at 800 bar for 3 min in lysis buffer (30 mM Tris, 200 mM NaCl, 1 mM GSH, pH 8.0) with 1 mM PSMF (AMRESCO). After the mixture was centrifuged at 18,000 rpm for an hour, the soluble protein fraction was then incubated with the Ni-NTA resin (GE Healthcare) for half an hour with gentle shaking. The mixture was then packed into a gravity column and washed with

https://doi.org/10.1021/jacsau.3c00696
JACS Au 2024, 4, 619−634

washing buffer (30 mM Tris, 200 mM NaCl, 1 mM GSH, 30 mM imidazole, pH 8.0). The MBP-8xHis-tagged Fhb7 protein was eluted from the column using elution buffer (30 mM Tris, 200 mM NaCl, 1 mM GSH, 200 mM imidazole, pH 8.0). The elution sample was exchanged into the buffer (30 mM Tris, 200 mM NaCl, 1 mM GSH, pH 8.0) by centrifuge. Then, the TEV enzyme was added to the sample and incubated overnight with gentle shaking to remove the MBP-8xHis tag from the Fhb7 protein. After TEV digestion, the sample flowed through a gravity column with Ni-NTA resin and amylose resin to remove the MBP-8xHis tag and TEV. The model in the flow-through was further purified using a Superdex 75 10/300 column (GE Healthcare) in the gel filtration buffer (30 mM Tris, 200 mM NaCl, 1 mM GSH, pH 8.0). Fractions containing purified Fhb7 were pooled and concentrated using an Amicon Ultra tube (Millipore, molecular weight cutoff of 10 kDa) to 9 mg/mL at 4 °C for crystallization. For expression of recombinant protein CtGST, the synthesized CtGST gene was cloned into vector pQLinkHx with an N-terminal 8xHis tag followed by a TEV cleavage site. Protein expression was performed with *E. coli* MC1061 harboring vector pQlinkHx-CtGST. The protein purification procedure was similar to the purification of Fhb7, except for adding 1 mM GSH throughout the purification to improve the protein stability. Purified CtGST was concentrated to 10 mg/mL at 4 °C using an Amicon Ultra filter (molecular weight cutoff of 10 kDa). Samples in every step were collected and analyzed by 10% SDS-PAGE (Figure S15A,B). For M10, we replaced regions 56−76 with peptide "ERVCKEIGAEP-SAFGLLKEGKPY" from CsGST83044 (PDB ID: 6j3h). The procedures of purifying M10 and CtGST-F76A were the same as the procedure of CtGST.

Crystallization, Data Collection, and Structure Determination

As for Fhb7, the purified protein (concentrated to 9 mg/mL) was used for initial and optimization crystallization conditions screening using the sitting-drop vapor-diffusion method. Crystals were grown at 16 °C for several days. The crystallization solution contains 0.1 M Tris, 1.2 M potassium sodium tartrate, and pH 8.0. For data collection, the crystals were transferred to a solution containing the same crystallization solution with 5% sucrose and plunged into liquid nitrogen. X-ray diffraction data of Fhb7 crystals were collected at SSRF (Shanghai Synchrotron Radiation Facility, beamline BL17U1). The diffraction data were processed by HKL2000.[57] We solved the structure using the molecular replacement method using the predicted model from AlphaFold.[58] The structure model of Fhb7 was then processed by Coot[59] and further refined by Phenix.[60] As for M10, the crystals of CtGST were grown at 16 °C for 2 days under 0.1 M Bis−Tris, pH 5.5, 0.2 M ammonium sulfate, and 25% M PEG 3350. As for CtGST and CtGST-F76A, 10 and 5 mg/mL of protein were used for initial and optimization crystallization conditions screening, respectively, with the same procedure as Fhb7. The crystals of CtGST were grown at 16 °C for 3 days under 0.1 M sodium acetate, pH 4.6, 1.2 M ammonium phosphate monobasic, and 0.3 M sodium iodide. The crystals of CtGST-F76A were grown at 16 °C for 3 days under 1.5 M lithium sulfate, 0.1 M trisodium citrate, pH 6.0. For data collection, the crystals were cryo-protected with crystallization solution supplemented with 30% ethylene glycol and substantially flashed frozen in liquid nitrogen. X-ray diffraction data of CtGST crystals were collected at SSRF (Shanghai Synchrotron Radiation Facility, beamline BL02U1). X-ray diffraction data of CtGST-F76A and M10 crystals were collected at SSRF (Shanghai Synchrotron Radiation Facility, beamline BL19U1). The diffraction data were processed by the HKL2000 package.[57] The structure of CtGST and M10 was determined by molecular replacement with Fhb7 structure as a search model using Phaser.[60] The structure of CtGST-F76A was determined by molecular replacement with CtGST structure as a search model using Phaser. The programs Phenix60 and Coot[59] were used for refinement. Data collection and structure refinement statistics are summarized in Table S1.

Fhb7 Random Mutagenesis Library Construction

The Fhb7 random mutagenesis library was constructed using error-prone PCR and MEGAWHOP PCR as described.[61,62] Briefly, the fragments of Fhb7 containing random mutations were obtained by error-prone PCR with primers Fhb7-F and Fhb7-R using rTaq DNA polymerase (Vazyme Biotech). The reaction mixture contained 0.2 mM each of dGTP and dATP, 1 mM each of dTTP and dCTP, 75 μM $MnCl_2$, 5.5 mM $MgCl_2$, 60 ng plasmid pQlinkHx-Fhb7 as template. Then, about 500 ng of the fragments were used as a megaprimer and 50 ng plasmid pTrc99a-$CysG^A$-Fhb7 as a template to perform MEGAWHOP PCR with KOD-Plus-Neo polymerase (TOYOBO). DpnI was added to the MEGAWHOP PCR products to digest the wild-type plasmid at 37 °C for 5 h and then inactivation at 80 °C for 20 min. The digestion products were transformed into *E. coli* MC1061 with electro-transformation. About 10^4 transformants were recovered. All the transformants were used for stability screening. Ten randomly picked clones from the library were sequenced and contained an average of 1−2 amino acid mutations per clone.

High-Throughput Screening of Random Mutation Library

We used a three-step screening method for library screening (Figure S11). In step one, all the transformants above were picked into 96 deep-well plates containing 500 μL of LB medium supplemented with 100 μg/mL of ampicillin and cultured at 37 °C, 300 rpm overnight. 100 μL of the cultures were transferred into new 96 deep-well plates containing 600 μL of fresh LB supplemented with 100 μg/mL of ampicillin and 1 mM IPTG. Then the plates were incubated at 37 °C, 300 rpm for 24 h. After that, the cultures were collected using centrifugation at 4000 rpm, 4 °C for 10 min, and washed with 1× PBS twice. Finally, 300 μL of 1× PBS was used to resuspend the cultures, and 200 μL of them were transferred into black 96-well plates. Transformants with higher red fluorescence were selected under UV by the eyes. About 150 transformants were selected and stored at −80 °C for the next screening step. In step two, the selected transformants were inoculated into a 3 mL of LB medium (containing 100 μg/mL of ampicillin) and incubated at 37 °C, 220 rpm overnight. 300 μL of the cultures were inoculated into fresh 3 mL of LB medium (containing 100 μg/mL of ampicillin and 1 mM IPTG) and cultured at 37 °C 220 rpm for 24 h. The medium was discarded after centrifugation at 8000 rpm, 4 °C for 10 min. Then the collected cultures were washed with 1× PBS twice and resuspended with 1 mL of 1× PBS. Next, 200 μL of the resuspended cultures were added to black 96-well plates. Then, the OD600 and fluorescence intensity (excitation filter at 360 nm and emission filter at 600 nm) of the cultures were determined using a Spark 10 M Multimode Microplate Reader (TECAN, Männedorf, Switzerland). The unit fluorescence intensity was calculated by dividing fluorescence intensity by OD600 and the relative fluorescence intensity was calculated by dividing the unit fluorescence intensity of selected transformants by the unit fluorescence intensity of wild-type. Seven transformants with higher relative fluorescence intensity were chosen for the next activity-based screening step. In step three, the plasmids of the seven transformants were obtained and sequenced (RuiBiotech). After that, genes of the transformants were cloned into vector pQlinkHx with MEGAWHOP PCR (See below) followed by protein expression, purification, activity, and Tm determination.

Consensus Site Analysis

The protein sequence of Fhb7 was used as an input file for consensus site analysis with the web tool Consensus Finder[50] (http://kazlab.umn.edu) using the following parameters: maximum sequences of 2000 for BLAST search, maximum e value of 1×10^{-3} for BLAST search, the minimum ratio of 7 for determining consensus, 3 iterations of ClustalW alignments, CD-Hit redundancy of 0.9. The output file of amino acid frequencies of the obtained 350 sequences from Consensus Finder was analyzed with GraphPad Prism 8.0.2. Ten residues of Fhb7 different from consensus sites in the corresponding positions with higher than 0.6 frequencies were selected for activity and Tm determination.

https://doi.org/10.1021/jacsau.3c00696
JACS Au 2024, 4, 619−634

Variant Construction

All the variants screened from the random mutation library and selected from consensus site analysis were constructed into pQlinkHx with MEGAWHOP PCR using primers in Table S2 for protein expression.[63] For the variants screened library, the gene fragments were amplified from obtained plasmids with primers Fhb7-F and Fhb7-R by PCR using TransStart FastPfu DNA polymerase (Transgene Biotech). About 300 ng of gene fragments were used as megaprimers to conduct MEGAWHOP PCR using 50 ng plasmid pQlinkHx-Fhb7 as a template. DpnI digestion was executed at 37 °C for 5 h and inactive at 80 °C for 20 min. The digestion products were transformed into *E. coli* MC1061 as described above. For the variants selected from consensus site analysis, the DNA fragments containing mutation sites were obtained by PCR using pQlinkHx-Fhb7 as a template and pQlinkHx-Seq-R as a reverse primer and the corresponding primer containing the mutation sites as a forward primer. The following MEGAWHOP PCR and transformation procedures were the same as the construction of variants screened from the library. All the sequences of variants were confirmed by Sanger sequencing (RuiBiotech).

Protein Purification for Activity Test and Tm Determination

The procedures of protein expression and purification for activity and the Tm test were similar to the expression and purification for crystallization. In brief, for protein expression, 1−2 L *E. coli* MC1061 containing target plasmids was grown at 37 °C, 220 rpm to OD600 value of 0.8−1.0 and followed by inducing at 18 °C for 20 h supplemented with 1 mM IPTG. Cells were harvested and lysed by ultrasonication for 15 min in enzyme buffer (20 mM NaH_2PO_4−Na_2HPO_4, 0.2 M NaCl, pH 8.0). After the mixture was centrifuged at 15,000 rpm, 4 °C for 30 min, the soluble protein fraction then flowed through Ni-NTA resin (GE Healthcare), washed with washing buffer (20 mM NaH_2PO_4−Na_2HPO_4, 0.2 M NaCl, 50 mM Imidazole, pH 8.0). The 8xHis-tagged Fhb7 protein was eluted from the column using elution buffer (20 mM NaH_2PO_4−Na_2HPO_4, 0.2 M NaCl, 250 mM Imidazole, pH 8.0). TEV was added to the elution products and gently shaken overnight at 4 °C to digest the His-tag. Then, digestion products flowed through Ni-NTA resin to remove the 8xHis tag and TEV. The samples in the flow-through were further purified using a Superdex increase 200 10/300 column (GE Healthcare) in the enzyme buffer (20 mM NaH_2PO_4−Na_2HPO_4, 0.2 M NaCl, pH 8.0). Fractions containing purified protein were pooled and concentrated using an Amicon Ultra tube (Millipore, molecular weight cutoff of 10 kDa) to 1−2 mg/mL at 4 °C. The purified proteins were frozen with liquid nitrogen and stored at −80 °C.

Tm Detection of Fhb7 and Variants

The Tm of Fhb7 and its variants were evaluated by Thermal Shift Assay[64] performed in a 96-well plate. Samples were diluted to a final protein concentration of 0.5 mg/mL in a solution consisting of enzyme buffer (20 mM NaH_2PO_4−Na_2HPO_4, 0.2 M NaCl, pH 8.0) and 2.5× SYPRO Orange (a 5000× SYPRO Orange preparation from Sigma-Aldrich ref S5692 was used as a stock solution) in a final volume of 25 μL. The samples were then subjected to thermal denaturation in a real-time PCR machine (Biorad) with a temperature gradient from 15 to 65 °C at a heating rate of 1 °C per minute. Protein unfolding was monitored by the increase in the fluorescence of the SYPRO Orange probe.

Activity Analysis

To determine the relative activity of different variants, reactions were performed with 100 μM DON and 1 mM fresh GSH at pH 8.0 and 30 °C for 6 min in a final volume of 100 μL that contained 5 μg proteins. The reaction condition was the same as relative activity determination to determine the retained activity after incubation at different temperatures. The 5 μg proteins were replaced by 5 μg incubated proteins at 35 °C for 5 min. Aliquots were quenched with 100 μL of ice-cold acetonitrile and centrifuged at 15,000*g*, 4 °C for 30 min. Supernatants were analyzed by reserve-phase UPLC-MS as described above.

$t_{1/2}$ Determination of Fhb7 and Its Variants

To determine the $t_{1/2}$ of Fhb7, V29P, and M10, the residual activities of enzymes incubated at 30 °C for various times were detected. Five μg proteins were added into 100 μL of enzyme buffer (20 mM NaH_2PO_4−Na_2HPO_4, 0.2 M NaCl, pH 8.0) and incubated at 30 °C at different times, and then these proteins were placed on ice immediately. After incubation on ice for 5 min, 100 μM DON and 1 mM fresh GSH were added to the reaction systems. The reactions were performed at 30 °C for 6 min. Aliquots were quenched with 100 μL of ice-cold acetonitrile and centrifuged at 15,000*g*, 4 °C for 30 min. Supernatants were analyzed by reserve-phase UPLC-MS as described above. For Fhb7, the incubation times at 30 °C were varied from 0 to 30 min and the incubation times of V29P and M10 varied from 0 min to 2 h and from 0 min to 72 h, respectively. The residual activity was shown as the activity of the enzyme incubated at 30 °C for a different time relative to the activity of the enzyme incubated for 0 min. Three parallel assays were routinely carried out.

Biochemical Property Analysis of Fhb7, V29P, and M10

To investigate the optimal reaction pH of Fhb7, enzymatic transformations were conducted in buffer with various pH in the ranges of 4.0−6.0 (50 mM citric acid−sodium citrate buffer), 6.0−9.0 (50 mM Na_2HPO_4−NaH_2PO_4 buffer), 8.0−9.0 (50 mM Tris−HCl buffer), and 9.5−11.0 (50 mM Na_2CO_3−$NaHCO_3$ buffer) using 5 μg proteins, 100 μM DON, and 1 mM GSH at 30 °C for 6 min. To investigate the optimal reaction temperature of Fhb7, V29P, and M10, reactions were carried out in Na_2HPO_4−NaH_2PO_4 buffer (pH 8.0) supplemented with 5 μg proteins, 100 μM DON and 1 mM GSH at various temperatures in the ranges 25−55 °C for 6 min. All the reactions were quenched with 100 μL of ice-cold acetonitrile and centrifuged at 15,000*g*, 4 °C for 30 min. Supernatants were analyzed by reserve-phase UPLC-MS as described above. The optimal reaction pH of Fhb7 is pH 8.0 in Na_2HPO_4−NaH_2PO_4 buffer (Figure S16A). The optimal reaction temperatures of Fhb7, V29P and M10 were 30 °C, 30 and 37 °C, respectively (Figure S16B).

Substrate Scope Analysis of Fhb7, V29P, and M10

To determine the relative activity of Fhb7, V29P, and M10 toward different trichothecenes (DON, 15-ADON, NIV, DAS, and T-2), reactions were performed with 100 μM one of the trichothecenes and 1 mM fresh GSH at pH 8.0 and 30 °C for 10 min in a final volume of 100 μL containing 5 μg of proteins. Aliquots were quenched with 100 μL of ice-cold acetonitrile and centrifuged at 15,000*g*, 4 °C for 30 min. Supernatants were analyzed by reserve-phase UPLC-MS as described above.

Protein Expression Level Analysis of Fhb7, V29P, and M10 in *E. coli* MC1061 and *B. subtilis* WB600

For analysis in *E. coli* MC1061, strains containing target genes were grown in 3 mL of LB medium at 37 °C, 220 rpm overnight. The cultures were inoculated at a ratio of 1% into 20 mL of fresh LB medium. The cells were grown at 37 °C to an OD_{600} value of 0.8−1.0 and induced at 30 °C by 1 mM IPTG for 20 h. The cells were collected by centrifugation at 4000 rpm for 10 min. Then, the cells were resuspended and the OD was adjusted to 2.0 with enzyme buffer (20 mM NaH_2PO_4−Na_2HPO_4, 0.2 M NaCl, pH 8.0). For analysis in *B. subtilis* WB600, plasmids were transformed into *B. subtilis* by electro-transformation according to the standard protocol. Colonies containing target plasmids were picked into 3 mL of LB medium and grown at 37 °C, 220 rpm overnight. The cultures were transferred to a 100 mL conical flask containing 40 mL of fresh LB medium at an inoculation rate of 1% and incubated at 37 °C, 220 rpm for 20 h. The cultures were collected and handled with the same procedure as *E. coli* MC1061; 40 μL cultures obtained above and 10 μL 5× protein loading buffer were mixed and heated at 100 °C for 10 min. Ten microliters of the mixtures were used for Western blot analysis. The protein expression level was determined by calculating the gray values of bands from Western blot results using ImageJ.[56]

https://doi.org/10.1021/jacsau.3c00696
JACS Au 2024, 4, 619−634

DON Detoxification Efficiency of Fhb7, V29P, and M10 *In Vivo*

To determine the DON detoxification efficiency of those engineering bacteria, the transformations were carried out with 200 μL cultures containing 0.5 mM DON and 2 mM fresh GSH at 37 °C for 0, 12, 24, 36, 48, 60, and 72 h, respectively. The reactions were quenched with 400 μL of ice-cold acetonitrile and centrifuged at 15,000g, 4 °C for 30 min. Residual DON in supernatants was analyzed by qTOF as described above.

Hydrogen−Deuterium Exchange Mass Spectrometry

To investigate the interactions between GSH, DON, and M10, 15 μm M10 protein was incubated with either 150 μm DON/GSH or an equal volume of DMSO as control at 30 °C for 1 h. The PAL3 System (LEAP Technologies,) was used for automatic and efficient sample preparation. Three microliters of protein were automatically dispensed into a vial and diluted 10-fold with the HDX labeling buffer (20 mM Tris−HCl, 75 mM NaCl, pH 7.4) at 10 °C and then quenched by adding an equal volume of quench buffer (4 M GnCl, 0.5 M TCEP, 100 mM Citric Acid, pH 2.3) for 1 min at 0.5 °C. The quenched sample was immediately injected into an immobilized protease type XIII/pepsin column (NovaBioAssays, cat. no. NBA2014005) for digestion at 4 °C. The digested peptides were trapped and separated by the AcclaimTM PepMap300 C18 column (Thermo Fisher Scientific, cat.no.163589) and ACQUITY UPLC Peptide CSH C18 Column (Waters, cat. no. 186002344) at 0 °C using the Ultimate NCS-3500 RSCL-pump system (Thermo Fisher Scientific, USA), respectively. The LC gradient was 0−2% over 4 min, 2−10% over 0.1 min, 10−28% over 9.9 min, 28−80% over 0.1 min, 80% over 1.9 min, 80−2% over 0.1 min, and 2% over 1.9 min.

Data were acquired using an Orbitrap Fusion Tribrid Mass Spectrometer (Thermo Fisher Scientific, USA) equipped with a heated electrospray ionization (HESI) source in positive ion mode. The tandem MS (MS/MS) data were analyzed by BioPharm Finder 2.0 software (Thermo Fisher Scientific, USA) for peptide identification and HDX-MS data were analyzed by HDExaminer (Sierra Analytics, Modesto, CA, USA). Statistical significance for the differential HDX data is determined by an unpaired *t*-test for each time point. All of the data were derived from at least three independent experiments.

Molecular Dynamics Simulations for the Catalytic Mechanism

The Fhb7-GSH complex was obtained according to the cocrystal structure of CsGST83044 with GSH (PDB ID: 6J3H) and the results of HDX-MS using Autodock Vina.[65] Then, the initial binding pose between DON and the Fhb7-GSH complex was obtained using Autodock Vina[65] (Table S6). MD simulations in explicit water were performed using the pmemd module of the Amber20 and AmberTools21 packages. For the protein scaffold, the ff14SB[66] parameters were applied. TIP3P[67] parameters were applied for water molecules. The gaff parameters were applied for GSH and DON. The transition state of the reaction between GSH and DON was obtained by Gaussian 16, and the geometric optimization and vibration analysis of the molecules were performed using B3LYP functional[68] and 6-31G(d) basis set. Only one expected imaginary frequency confirmed we found the correct transition state. The partial charge of GSH and DON was developed to fit the transition state's electrostatic potential generated at HF/6-31G(d) level.[69] We used Gaussian16 to obtain the transition state between GSH and DON. For the MD simulation of the GSH-DON-Fhb7 system, constraints with 500 kcal mol^{-1} Å^{-2} or 500 kcal mol^{-1} rad^{-2} were applied to maintain the transition state. Each protein complex was immersed in a pre-equilibrated octahedral box with a 12 Å buffer of TIP3P water molecules using Leap. All systems were neutralized by adding explicit counterions (Na^+ or Cl^-). A 10 Å cutoff was applied to Lennard−Jones and electrostatic interactions. MD simulations used the following steps: (1) minimization was performed with a maximum cycle of 10,000 and with the steepest descent algorithm for the first 5000 cycles. Positional restraints of 0.5 kcal mol^{-1} Å^{-2} were applied on protein and ligands. (2) Minimization was performed with a maximum cycle of 10,000 and with the steepest descent algorithm for the first 5000 cycles. (3) A 1 ns heating process was performed with a periodic boundary for constant volume with the SHAKE algorithm (all hydrogen bonds were constrained). Temperature increased from 0 to 303 K with Langevin dynamics with the collision frequency of 2 ps^{-1}. Positional restraints of 0.5 kcal mol^{-1} Å^{-2} were applied on protein and ligands. (4) A 1 ns equilibrium process was performed with a periodic boundary for a constant pressure of 1 atm and with a constant temperature of 303 K to adjust the system's density. (5) A 500 ns production was performed with a periodic boundary for constant pressure 1 atm and temperature of 303 K.

Molecular Dynamics Simulations for Thermostability analysis

The initial conformations for MD simulations were obtained from our crystal structure. The missing segments were predicted using Alphafold2. All-atom MD simulations were performed using the Amber18 package and the AMBER ff14sb force field was used for the protein. The systems were solvated using TIP3P water with a thickness of 15 Å and the Na^+ and Cl^- ions were used as counterions to neutralize the systems. The systems were initially refined using 500 steepest descent steps before switching to conjugate gradient energy minimization and gradually heated to 300 K within 2 ns. The positional restraints were exerted on the protein's backbone with a weight of 10 kcal/mol/Å^2 during the energy minimization and heating. Then, the restraints were released gradually within six equilibration steps under a constant pressure and temperature (*NPT*) ensemble. The hydrogen mass repartitioning was set to 4 amu to enable an integration step of 4 fs for the simulations. The production runs were conducted using a 12 Å cutoff distance for the Lennard−Jones interactions, and the Particle Mesh Ewald (PME) summation method was used for calculating Coulomb interactions. Five ×2000 ns production runs were conducted for wildtype and mutant of Fhb7.

■ ASSOCIATED CONTENT

Supporting Information

The Supporting Information is available free of charge at https://pubs.acs.org/doi/10.1021/jacsau.3c00696.

Overall structure and positions; relative activity; sequence alignment; UPLC-MS analysis; MD simulation; directed evolution; protein expression level; and transition state of GSH and DON (PDF)

■ AUTHOR INFORMATION

Corresponding Authors

Junyu Xiao − *School of Life Sciences and Academy for Advanced Interdisciplinary Studies, Peking University, Beijing 100871, China*; Email: junyuxiao@pku.edu.cn

Xiaoguang Lei − *Beijing National Laboratory for Molecular Sciences, Key Laboratory of Bioorganic Chemistry and Molecular Engineering of Ministry of Education, Department of Chemical Biology, College of Chemistry and Molecular Engineering, and Peking-Tsinghua Center for Life Sciences and Academy for Advanced Interdisciplinary Studies, Peking University, Beijing 100871, China; Institute for Cancer Research, Shenzhen Bay Laboratory, Shenzhen 518107, China*; orcid.org/0000-0002-0380-8035; Email: xglei@pku.edu.cn

Authors

Jun Yang − *Academy for Advanced Interdisciplinary Studies and Beijing National Laboratory for Molecular Sciences, Key Laboratory of Bioorganic Chemistry and Molecular Engineering of Ministry of Education, Department of*

https://doi.org/10.1021/jacsau.3c00696
JACS Au 2024, 4, 619−634

Chemical Biology, College of Chemistry and Molecular Engineering, and Peking-Tsinghua Center for Life Sciences, Peking University, Beijing 100871, China

Kai Liang − *School of Life Sciences, Peking University, Beijing 100871, China*

Han Ke − *Beijing National Laboratory for Molecular Sciences, Key Laboratory of Bioorganic Chemistry and Molecular Engineering of Ministry of Education, Department of Chemical Biology, College of Chemistry and Molecular Engineering, and Peking-Tsinghua Center for Life Sciences, Peking University, Beijing 100871, China*

Yuebin Zhang − *Laboratory of Molecular Modeling and Design, State Key Laboratory of Molecular Reaction Dynamics, Dalian Institute of Chemical Physics, Chinese Academy of Sciences, Dalian 116023, China*

Qian Meng − *Analytical Research Center for Organic and Biological Molecules, State Key Laboratory of Drug Research, Shanghai Institute of Materia Medica, Chinese Academy of Sciences, Shanghai 201203, China*

Lei Gao − *Beijing National Laboratory for Molecular Sciences, Key Laboratory of Bioorganic Chemistry and Molecular Engineering of Ministry of Education, Department of Chemical Biology, College of Chemistry and Molecular Engineering, and Peking-Tsinghua Center for Life Sciences, Peking University, Beijing 100871, China*

Junping Fan − *Beijing National Laboratory for Molecular Sciences, Key Laboratory of Bioorganic Chemistry and Molecular Engineering of Ministry of Education, Department of Chemical Biology, College of Chemistry and Molecular Engineering, and Peking-Tsinghua Center for Life Sciences, Peking University, Beijing 100871, China*

Guohui Li − *Laboratory of Molecular Modeling and Design, State Key Laboratory of Molecular Reaction Dynamics, Dalian Institute of Chemical Physics, Chinese Academy of Sciences, Dalian 116023, China;* orcid.org/0000-0001-8223-705X

Hu Zhou − *Analytical Research Center for Organic and Biological Molecules, State Key Laboratory of Drug Research, Shanghai Institute of Materia Medica, Chinese Academy of Sciences, Shanghai 201203, China; University of Chinese Academy of Sciences, Beijing 100049, China;* orcid.org/0000-0001-7006-4737

Complete contact information is available at: https://pubs.acs.org/10.1021/jacsau.3c00696

Author Contributions

X.L. initiated and managed the whole project; J.Y. and X.L. designed the experiments; J.Y. performed most of the experiments with the help of L.G. and J.F.; K.L. performed the crystal structure study under the guidance of J.X.; H.K. and Y.Z. conducted the computational analysis under the guidance of G.L.; Q.M. performed the HDX-MS under the guidance of H.Z.; J.Y. and X.L. wrote the manuscript with inputs from all the authors. J.Y. and K.L. contributed equally.

Funding

This work was supported by the National Key Research and Development Plan (2021YFC2102900 to L.G.), the National Natural Science Foundation of China (22193073 and 92253305 to X.L.; 22101009 to L.G.; 22177006 to J.F.; 31700647 to Y.Z.), and the Beijing Outstanding Young Scientist Program (BJJWZYJH01201910001001 to X.L.). This work is also supported by the New Cornerstone Science Foundation through the XPLORER PRIZE and the Beijing National Laboratory for Molecular Sciences (grant BNLMS-CXX-202106).

Notes

The authors declare no competing financial interest.

■ ACKNOWLEDGMENTS

We thank C. P. Gao (Peking University) for assistance with X-ray data analysis and K. Wu (Peking University) for help with data analysis. We are grateful to the High-performance Computing Platform of Peking University for structure prediction. We are thankful to the staff members of the Shanghai Synchrotron Radiation Facility (beamline BL17U1 and BL02U1) for their support during X-ray data collection. We also thank National Center for Protein Sciences at Peking University in Beijing, China and Dr. T. Wei for assistance with crystal screening.

■ ABBREVIATIONS

DON, deoxynivalenol; FHB, *Fusarium* head blight

■ REFERENCES

(1) Timmusk, S.; Nevo, E.; Ayele, F.; Noe, S.; Niinemets, Y. Fighting Fusarium Pathogens in the Era of Climate Change: A Conceptual Approach. *Pathogens* **2020**, *9*, 419.

(2) Bai, G.; Shaner, G. Management and resistance in wheat and barley to Fusarium head blight. *Annu. Rev. Phytopathol.* **2004**, *42*, 135−161.

(3) Liu, C.; Van der Fels-Klerx, H. J. Quantitative Modeling of Climate Change Impacts on Mycotoxins in Cereals: A Review. *Toxins (Basel)* **2021**, *13*, 276.

(4) Garreau de Loubresse, N.; Prokhorova, I.; Holtkamp, W.; Rodnina, M. V.; Yusupova, G.; Yusupov, M. Structural basis for the inhibition of the eukaryotic ribosome. *Nature* **2014**, *513*, 517−522.

(5) Wang, W.; Zhu, Y.; Abraham, N.; Li, X. Z.; Kimber, M.; Zhou, T. The Ribosome-Binding Mode of Trichothecene Mycotoxins Rationalizes Their Structure-Activity Relationships. *Int. J. Mol. Sci.* **2021**, *22*, 1604.

(6) Trail, F. For blighted waves of grain: Fusarium graminearum in the postgenomics era. *Plant Physiol.* **2009**, *149*, 103−110.

(7) Bai, G. H.; Desjardins, A. E.; Plattner, R. D. Deoxynivalenol-nonproducing Fusarium graminearum causes initial infection, but does not cause disease spread in wheat spikes. *Mycopathologia* **2002**, *153*, 91−98.

(8) Yao, Y.; Long, M. The biological detoxification of deoxynivalenol: A review. *Food Chem. Toxicol.* **2020**, *145*, No. 111649.

(9) Hathout, A. S.; Aly, S. E. Biological detoxification of mycotoxins: a review. *Annals of Microbiology* **2014**, *64*, 905−919.

(10) Hou, S.; Ma, J.; Cheng, Y.; Wang, H.; Sun, J.; Yan, Y. The toxicity mechanisms of DON to humans and animals and potential biological treatment strategies. *Crit. Rev. Food Sci. Nutr.* **2023**, *63*, 790−812.

(11) Chen, L.; Yang, J.; Wang, H.; Yang, X.; Zhang, C.; Zhao, Z.; Wang, J. NX toxins: New threat posed by Fusarium graminearum species complex. *Trends Food Sci. Technol.* **2022**, *119*, 179−191.

(12) Karlovsky, P.; Suman, M.; Berthiller, F.; Meester, J. D.; Eisenbrand, G.; Perrin, I.; Oswald, I. P.; Speijers, G.; Chiodini, A.; Recker, T.; et al. Impact of food processing and detoxification treatments on mycotoxin contamination. *Mycotoxin Res.* **2016**, *32*, 179−205.

(13) He, J.; Zhou, T.; Young, J. C.; Boland, G. J.; Scott, P. M. Chemical and biological transformations for detoxification of trichothecene mycotoxins in human and animal food chains: a review. *Trends Food Sci. Technol.* **2010**, *21*, 67−76.

(14) Awad, W. A.; Ghareeb, K.; Böhm, J.; Zentek, J. Decontamination and detoxification strategies for the Fusarium mycotoxin

deoxynivalenol in animal feed and the effectiveness of microbial biodegradation. *Food Addit. Contam. Part A Chem. Anal. Control Expo. Risk Assess.* **2010**, *27*, 510−520.
(15) Völkl, A.; Vogler, B.; Schollenberger, M.; Karlovsky, P. Microbial detoxification of mycotoxin deoxynivalenol. *J. Basic Microbiol.* **2004**, *44*, 147−156.
(16) Karlovsky, P. Biological detoxification of the mycotoxin deoxynivalenol and its use in genetically engineered crops and feed additives. *Appl. Microbiol. Biotechnol.* **2011**, *91*, 491−504.
(17) Ben Taheur, F.; Kouidhi, B.; Al Qurashi, Y. M. A.; Ben Salah-Abbès, J.; Chaieb, K. Review: Biotechnology of mycotoxins detoxification using microorganisms and enzymes. *Toxicon* **2019**, *160*, 12−22.
(18) Lyagin, I.; Efremenko, E. Enzymes for Detoxification of Various Mycotoxins: Origins and Mechanisms of Catalytic Action. *Molecules* **2019**, *24*, 2362.
(19) Pinto, A.; De Pierri, C. R.; Evangelista, A. G.; Gomes, A.; Luciano, F. B. Deoxynivalenol: Toxicology, Degradation by Bacteria, and Phylogenetic Analysis. *Toxins (Basel)* **2022**, *14*, 90.
(20) Huang, J. Q.; Fang, X.; Tian, X.; Chen, P.; Lin, J. L.; Guo, X. X.; Li, J. X.; Fan, Z.; Song, W. M.; Chen, F. Y.; et al. Aromatization of natural products by a specialized detoxification enzyme. *Nat. Chem. Biol.* **2020**, *16*, 250−256.
(21) Pierron, A.; Mimoun, S.; Murate, L. S.; Loiseau, N.; Lippi, Y.; Bracarense, A.; Schatzmayr, G.; He, J. W.; Zhou, T.; Moll, W. D.; et al. Microbial biotransformation of DON: molecular basis for reduced toxicity. *Sci. Rep.* **2016**, *6*, 29105.
(22) Khatibi, P. A.; Montanti, J.; Nghiem, N. P.; Hicks, K. B.; Berger, G.; Brooks, W. S.; Griffey, C. A.; Schmale, D. G., 3rd Conversion of deoxynivalenol to 3-acetyldeoxynivalenol in barley-derived fuel ethanol co-products with yeast expressing trichothecene 3-O-acetyltransferases. *Biotechnol. Biofuels* **2011**, *4*, 26.
(23) Ohsato, S.; Ochiai-Fukuda, T.; Nishiuchi, T.; Takahashi-Ando, N.; Koizumi, S.; Hamamoto, H.; Kudo, T.; Yamaguchi, I.; Kimura, M. Transgenic rice plants expressing trichothecene 3-O-acetyltransferase show resistance to the Fusarium phytotoxin deoxynivalenol. *Plant Cell Rep.* **2007**, *26*, 531−538.
(24) Garvey, G. S.; McCormick, S. P.; Rayment, I. Structural and functional characterization of the TRI101 trichothecene 3-O-acetyltransferase from Fusarium sporotrichioides and Fusarium graminearum: kinetic insights to combating Fusarium head blight. *J. Biol. Chem.* **2008**, *283*, 1660−1669.
(25) Poppenberger, B.; Berthiller, F.; Lucyshyn, D.; Sieberer, T.; Schuhmacher, R.; Krska, R.; Kuchler, K.; Glossl, J.; Luschnig, C.; Adam, G. Detoxification of the Fusarium mycotoxin deoxynivalenol by a UDP-glucosyltransferase from Arabidopsis thaliana. *J. Biol. Chem.* **2003**, *278*, 47905−47914.
(26) Schweiger, W.; Boddu, J.; Shin, S.; Poppenberger, B.; Berthiller, F.; Lemmens, M.; Muehlbauer, G. J.; Adam, G. Validation of a candidate deoxynivalenol-inactivating UDP-glucosyltransferase from barley by heterologous expression in yeast. *Mol. Plant-Microbe Interact.* **2010**, *23*, 977−986.
(27) Shin, S.; Torres-Acosta, J. A.; Heinen, S. J.; McCormick, S.; Lemmens, M.; Kovalsky Paris, M. P.; Berthiller, F.; Adam, G.; Muehlbauer, G. J. Transgenic Arabidopsis thaliana expressing a barley UDP-glucosyltransferase exhibit resistance to the mycotoxin deoxynivalenol. *J. Exp. Bot.* **2012**, *63*, 4731−4740.
(28) Wetterhorn, K. M.; Gabardi, K.; Michlmayr, H.; Malachova, A.; Busman, M.; McCormick, S. P.; Berthiller, F.; Adam, G.; Rayment, I. Determinants and Expansion of Specificity in a Trichothecene UDP-Glucosyltransferase from Oryza sativa. *Biochemistry* **2017**, *56*, 6585−6596.
(29) He, W. J.; Zhang, L.; Yi, S. Y.; Tang, X. L.; Yuan, Q. S.; Guo, M. W.; Wu, A. B.; Qu, B.; Li, H. P.; Liao, Y. C. An aldo-keto reductase is responsible for Fusarium toxin-degrading activity in a soil Sphingomonas strain. *Sci. Rep.* **2017**, *7*, 9549.
(30) Carere, J.; Hassan, Y. I.; Lepp, D.; Zhou, T. The Identification of DepB: An Enzyme Responsible for the Final Detoxification Step in the Deoxynivalenol Epimerization Pathway in Devosia mutans 17−2-E-8. *Front. Microbiol.* **2018**, *9*, 1573.
(31) Carere, J.; Hassan, Y. I.; Lepp, D.; Zhou, T. The enzymatic detoxification of the mycotoxin deoxynivalenol: identification of DepA from the DON epimerization pathway. *Microb. Biotechnol.* **2018**, *11*, 1106−1111.
(32) He, W. J.; Shi, M. M.; Yang, P.; Huang; Zhao, Y.; Wu, A. B.; Dong, W. B.; Li, H. P.; Zhang, J. B.; Liao, Y. C. A quinone-dependent dehydrogenase and two NADPH-dependent aldo/keto reductases detoxify deoxynivalenol in wheat via epimerization in a Devosia strain. *Food Chem.* **2020**, *321*, No. 126703.
(33) Loi, M.; Fanelli, F.; Liuzzi, V. C.; Logrieco, A. F.; Mulè, G. Mycotoxin Biotransformation by Native and Commercial Enzymes: Present and Future Perspectives. *Toxins* **2017**, *9*, 111.
(34) Vanhoutte, I.; Audenaert, K.; De Gelder, L. Biodegradation of Mycotoxins: Tales from Known and Unexplored Worlds. *Front. Microbiol.* **2016**, *7*, 561.
(35) Fuchs, E.; Binder, E.; Heidler, D.; Krska, R. Characterisation of metabolites after the microbial degradation of A- and B-trichothecenes by BBSH 797. *Mycotoxin Res.* **2000**, *16*, 66−69.
(36) Fuchs, E.; Binder, E. M.; Heidler, D.; Krska, R. Structural characterization of metabolites after the microbial degradation of type A trichothecenes by the bacterial strain BBSH 797. *Food Addit. Contam.* **2002**, *19*, 379−386.
(37) Binder, J.; Horvath, E. M.; Schatzmayr, G.; Ellend, N.; Danner, H.; Krska, R.; Braun, R. Screening for deoxynivalenol-detoxifying anaerobic rumen microorganisms. *Cereal Res. Commun.* **1997**, *25*, 343−346.
(38) Wang, H.; Sun, S.; Ge, W.; Zhao, L.; Hou, B.; Wang, K.; Lyu, Z.; Chen, L.; Xu, S.; Guo, J.; et al. Horizontal gene transfer of Fhb7 from fungus underlies Fusarium head blight resistance in wheat. *Science* **2020**, *368*, No. eaba5435.
(39) Liu, Q.; Xun, G.; Feng, Y. The state-of-the-art strategies of protein engineering for enzyme stabilization. *Biotechnol. Adv.* **2019**, *37*, 530−537.
(40) Osman, W. H. W.; Mikami, B.; Saka, N.; Kondo, K.; Lin, M. I.; Nagata, T.; Katahira, M. Identification of key residues for activities of atypical glutathione S-transferase of Ceriporiopsis subvermispora, a selective degrader of lignin in woody biomass, by crystallography and functional mutagenesis. *Int. J. Biol. Macromol.* **2019**, *132*, 222−229.
(41) Morel, M.; Meux, E.; Mathieu, Y.; Thuillier, A.; Chibani, K.; Harvengt, L.; Jacquot, J. P.; Gelhaye, E. Xenomic networks variability and adaptation traits in wood decaying fungi. *Microb. Biotechnol.* **2013**, *6*, 248−263.
(42) Morel, M.; Ngadin, A. A.; Droux, M.; Jacquot, J. P.; Gelhaye, E. The fungal glutathione S-transferase system. Evidence of new classes in the wood-degrading basidiomycete Phanerochaete chrysosporium. *Cell. Mol. Life Sci.* **2009**, *66*, 3711−3725.
(43) Osman, W. H.; Mikami, B.; Saka, N.; Kondo, K.; Nagata, T.; Katahira, M. Structure of a serine-type glutathione S-transferase of Ceriporiopsis subvermispora and identification of the enzymatically important non-canonical residues by functional mutagenesis. *Biochem. Biophys. Res. Commun.* **2019**, *2019* (510), 177−183.
(44) Osman, W. H.; Lin, M.-I.; Kondo, K.; Nagata, T.; Katahira, M. Characterization of the glutathione S-transferases that belong to the GSTFuA class in Ceriporiopsis subvermispora: Implications in intracellular detoxification and metabolism of wood-derived compounds. *Int. J. Biol. Macromol.* **2018**, *113*, 1158−1166.
(45) Winayanuwattikun, P.; Ketterman, A. J. An electron-sharing network involved in the catalytic mechanism is functionally conserved in different glutathione transferase classes. *J. Biol. Chem.* **2005**, *280*, 31776−31782.
(46) Ren, C.; Wen, X.; Mencius, J.; Quan, S. An enzyme-based biosensor for monitoring and engineering protein stability in vivo. *Proc. Natl. Acad. Sci. U. S. A.* **2021**, *118*, No. e2101618118.
(47) Studer, R. A.; Christin, P.-A.; Williams, M. A.; Orengo, C. A. Stability-activity tradeoffs constrain the adaptive evolution of RubisCO. *Proc. Natl. Acad. Sci. U. S. A.* **2014**, *111*, 2223−2228.

https://doi.org/10.1021/jacsau.3c00696
JACS Au 2024, 4, 619−634

(48) Siddiqui, K. S. Defying the activity-stability trade-off in enzymes: taking advantage of entropy to enhance activity and thermostability. *Crit. Rev. Biotechnol.* **2017**, *37*, 309−322.
(49) Yu, H.; Dalby, P. A. Exploiting correlated molecular-dynamics networks to counteract enzyme activity-stability trade-off. *Proc. Natl. Acad. Sci. U. S. A.* **2018**, *115*, E12192−E12200.
(50) Jones, B. J.; Kan, C. N.; Luo, C.; Kazlauskas, R. J. Consensus Finder web tool to predict stabilizing substitutions in proteins. *Methods in Enzymol.* **2020**, *643*, 129−148.
(51) Porebski, B. T.; Buckle, A. M. Consensus protein design. *Protein Eng. Des. Sel.* **2016**, *29*, 245−251.
(52) Sternke, M.; Tripp, K. W.; Barrick, D. Consensus sequence design as a general strategy to create hyper stable, biologically active proteins. *Proc. Natl. Acad. Sci. U. S. A.* **2019**, *116*, 11275−11284.
(53) Jones, B. J.; Lim, H. Y.; Huang, J.; Kazlauskas, R. J. Comparison of Five Protein Engineering Strategies for Stabilizing an α/β-Hydrolase. *Biochemistry* **2017**, *56*, 6521−6532.
(54) Janik, E.; Niemcewicz, M.; Podogrocki, M.; Ceremuga, M.; Stela, M.; Bijak, M. T-2 Toxin-The Most Toxic Trichothecene Mycotoxin: Metabolism, Toxicity, and Decontamination Strategies. *Molecules* **2021**, *26*, 6868.
(55) Średnicka, P.; Juszczuk-Kubiak, E.; Wójcicki, M.; Akimowicz, M.; Roszko, M. Probiotics as a biological detoxification tool of food chemical contamination: A review. *Food Chem. Toxicol.* **2021**, *153*, No. 112306.
(56) Schneider, C. A.; Rasband, W. S.; Eliceiri, K. W. NIH Image to ImageJ: 25 years of image analysis. *Nat. methods* **2012**, *9*, 671−675.
(57) Otwinowski, Z.; Minor, W. *Methods in Enzymology*; Academic Press, 1997; vol *276*, pp 307−326.
(58) Jumper, J.; Evans, R.; Pritzel, A.; Green, T.; Figurnov, M.; Ronneberger, O.; Tunyasuvunakool, K.; Bates, R.; Zidek, A.; Potapenko, A.; et al. Highly accurate protein structure prediction with AlphaFold. *Nature* **2021**, *596*, 583−589.
(59) Emsley, P.; Lohkamp, B.; Scott, W. G.; Cowtan, K. Features and development of Coot. *Acta Crystallogr. D Biol. Crystallogr.* **2010**, *66*, 486−501.
(60) Adams, P. D.; Afonine, P. V.; Bunkoczi, G.; Chen, V. B.; Davis, I. W.; Echols, N.; Headd, J. J.; Hung, L. W.; Kapral, G. J.; Grosse-Kunstleve, R. W.; et al. PHENIX: a comprehensive Python-based system for macromolecular structure solution. *Acta Crystallogr. D Biol. Crystallogr.* **2010**, *66*, 213−221.
(61) Miyazaki, K. MEGAWHOP cloning: a method of creating random mutagenesis libraries via megaprimer PCR of whole plasmids. *Methods Enzymol.* **2011**, *498*, 399−406.
(62) Miyazaki, K.; Takenouchi, M. Creating random mutagenesis libraries using megaprimer PCR of whole plasmid. *Biotechniques* **2002**, *33*, 1036−1038.
(63) Gao, L.; Zou, Y.; Liu, X.; Yang, J.; Du, X.; Wang, J.; Yu, X.; Fan, J.; Jiang, M.; Li, Y.; et al. Enzymatic control of endo- and exo-stereoselective Diels−Alder reactions with broad substrate scope. *Nat. Catal.* **2021**, *4*, 1059−1069.
(64) Dupeux, F.; Röwer, M.; Seroul, G.; Blot, D.; Márquez, J. A. A thermal stability assay can help to estimate the crystallization likelihood of biological samples. *Acta Crystallogr. D Biol. Crystallogr.* **2011**, *67*, 915−919.
(65) Trott, O.; Olson, A. J. AutoDock Vina: Improving the speed and accuracy of docking with a new scoring function, efficient optimization, and multithreading. *J. Comput. Chem.* **2010**, *31*, 455−461.
(66) Maier, J. A.; Martinez, C.; Kasavajhala, K.; Wickstrom, L.; Hauser, K. E.; Simmerling, C. ff14SB: Improving the Accuracy of Protein Side Chain and Backbone Parameters from ff99SB. *J. Chem. Theory. Comput.* **2015**, *11*, 3696−3713.
(67) Jorgensen, W. L.; Chandrasekhar, J.; Madura, J. D.; Impey, R. W.; Klein, M. L. Comparison of simple potential functions for simulating liquid water. *J. Chem. Phys.* **1983**, *79*, 926−935.
(68) Stephens, P. J.; Devlin, F. J.; Chabalowski, C. F.; Frisch, M. J. Ab Initio Calculation of Vibrational Absorption and Circular Dichroism Spectra Using Density Functional Force Fields. *J. Phys. Chem.* **1994**, *98*, 11623−11627.
(69) Bayly, C. I.; Cieplak, P.; Cornell, W.; Kollman, P. A. A well-behaved electrostatic potential based method using charge restraints for deriving atomic charges: the RESP model. *J. Phys. Chem.* **1993**, *97*, 10269−10280.

https://doi.org/10.1021/jacsau.3c00696
JACS Au 2024, 4, 619−634